

The MEso-SCAle Particle Transport model (MESCAPT) for
studying sediment dynamics during storms and tsunamis

Wei Cheng

Dissertation submitted to the Faculty of the
Virginia Polytechnic Institute and State University
in partial fulfillment of the requirements for the degree of

Doctor of Philosophy

in

Geophysics

Robert Weiss, Chair

Panayiotis Diplas

Scott King

Brian W. Romans

Nina Stark

Nov 12, 2015

Blacksburg, Virginia

Keywords: Tsunami, Storm, Sediment Transport, Meso-scale Particles, Numerical
Modeling

Copyright 2015, Wei Cheng

The MEso-SCAle Particle Transport model (MESCAPT) for studying
sediment dynamics during storms and tsunamis

Wei Cheng

Abstract

Tsunamis and storms are the most devastating coastal hazards that can cause great loss of life and infrastructure damage. To assess tsunami and storm hazard, the magnitude and frequency of each type of event are needed. However, major tsunamis and storms are very infrequent, especially tsunamis, and the only reliable record is the deposits they leave behind. Tsunami and storm deposits can be used to calculate the magnitudes of the respective event, and to contribute to the hazard frequency where there is no historical records. Therefore, for locations where both events could occur, it is crucial to differentiate between the two types of events. Existing studies on the similarities and differences between the two types of deposits all suffer from paucity of the number of events and field data, and a wide range of initial conditions, and thus an unequivocal set of distinguishing deposit characteristics has not been identified yet. In this study, we aim to tackle the problem with the MEso-SCAle Particle Transport model (MESCAPT) that combines the advantages of concentration-based Eulerian methods and particle-based method. The advantage of the former is efficiency and the latter is detailed sediment transport and deposit information. Instead of modeling individual particles, we assume that a group of sediment grains travel and deposit together, which is called a meso-scale particle. This allows simulation domains that are large enough for tsunami and storm wave propagation and inundation. The sediment transport model is coupled with a hydrodynamic model based on the shallow water equations. Simulation results of a case study show good agreements with field measurements of deposits left behind by the 2004 Indian Ocean

Tsunami. Idealized tsunami and storm case studies demonstrate the model's capabilities of reproducing morphological changes, as well as microscopic grain-size trends.

Contents

1	Introduction	1
2	On sediment extent and runup of tsunami waves	11
2.1	Introduction	12
2.2	Theoretical Background and Model Setup	16
2.2.1	The MOST code	16
2.2.2	Sediment Model	17
2.2.3	Model Setup	19
2.3	Results	20
2.4	Discussion and Conclusions	24
3	The Role of shoreline and bottom type dynamics in understanding barrier island vulnerability and resiliency	28

CONTENTS

3.1	Introduction	28
3.2	Hurricane Sandy and study locations	29
3.3	Simulations	30
3.3.1	Computational grid	31
3.3.2	Vegetation layer setup in XBeach	32
3.3.3	Model setup	33
3.3.4	Simulation results	34
3.3.5	Discussion	38
4	The MEso-SCALE Particle Transport model (MESCAPT) for studying sediment dynamics during storms and tsunamis	41
4.1	Introduction	43
4.2	Theoretical Background	45
4.2.1	The Meso-scale Concept	45
4.2.2	Governing Equations for Meso-scale Particle Transport	49
4.2.3	Hydrodynamic Model	57
4.2.4	Work Flow	63
4.3	Sediment Transport Validation	64

CONTENTS

4.4	Model Applications	68
4.4.1	Model Setup and Initial Conditions	68
4.4.2	Results	70
4.4.3	Discussion	75
4.5	Model Limitations and Potential Future Directions	76
4.6	Conclusions	77
5	Future Work	82
A	Hydrodynamic Model Validation	97
A.1	Solitary Wave Running Up on A Canonical Beach (continued)	97
A.2	Analytical Solution of Landslide Generated Tsunami	98

List of Figures

2.1 A sketch of the bathymetry and solitary wave for the MOST-1D tsunami simulations. The gray region shows the sea water covering the constant depth and sloping beach. Various dry slopes are connected to the right edge of shelf. The initial sea level is set at the conjunction of shelf and beach. h is solitary wave height, D is constant water depth, $s = \cot(\beta)$ is the beach slope where β is the angle of the beach, and $S_s = \cot(\beta_s)$ is shelf slope. Note that this figure is not plotted to scale. 19

2.2 Deposition ratio versus normalized beach slope $\tilde{s} = s S_s^{-1}$ and normalized initial wave height $\tilde{h} = h D^{-1}$. (a) shows an envelope where smoothed deposition ratio data at \tilde{s}_{min} and \tilde{s}_{max} define the upper and lower boundaries respectively. (b) shows again an envelope of deposition ratio, except that \tilde{s} is on the x-axis and \tilde{h}_{min} and \tilde{h}_{max} define the boundaries. 21

LIST OF FIGURES

2.3	Contour plot showing deposition ratio as a function of normalized beach slope \tilde{s} and initial wave height \tilde{h} . The equation is described in Eq. (2.6). This two dimensional plot better illustrates the tendency of deposition ratio saturation interval to increase as slope becomes steeper. Most of the parameter space exhibits a deposition ratio of $\xi > 0.9$, indicating sediment extents commonly approximates tsunami inundation.	23
3.1	Lidar and etopo profile lines in the Moriches Bay area.	32
3.2	Lidar profiles of the Moriches area.	33
3.3	Idealized combined profile of the Moriches Bay area.	34
3.4	Vegetation layer setup. Plot is showing the percentage for grain size class #1. The top layer contains only grain size #2 (blue), and everywhere else #1 (yellow).	35
3.5	Storm surge time series.	36
3.6	Final bed profiles for each sedcal for 50 m berm width.	36
3.7	Final bed profiles for each sedcal for 75 m berm width.	37
3.8	Final bed profiles for each sedcal for 100 m berm width.	37
3.9	Final bed profiles for each sedcal for 125 m berm width.	38
3.10	Final bed profiles for each sedcal for 150 m berm width.	39

LIST OF FIGURES

3.11	Overwash deposition volume vs. berm width.	39
3.12	Dune height eroded vs. berm width.	40
4.1	Illustration of comparison between conventional grid-based methods for sediment transport (a) and meso-scale particles (b). Black dots denote sediment grains, and colored circles denote meso-scale particles of different sizes. Colored grid in (a) shows the concentration of the sediments, with darker blue indicating higher concentration.	46
4.2	Deposition grid with illustrations of erosion and deposition of meso-scale particles. Dark grey color denotes solid layer. Blue rectangles form the deposition grid. Beige color denotes deposits. Red solid circle is a newly generated particle. Green solid circle is a particle that will be deposited.	52
4.3	Inverted velocity profile for an initial solitary wave of amplitude 0.4m. Top pane shows the shallow water velocity for this wave. Bottom pane is a contour plot of the velocity magnitude.	60
4.4	Comparison between numerical simulation results and experimental data of an $h/D = 0.0185$ non-breaking solitary wave running up on a single slope. Results show very good correlation.	62
4.5	Model work flow.	64

LIST OF FIGURES

4.6 Simulation setup for the 2004 Indian Ocean Tsunami. Data are digitized from Fig. 1 in Apotsos et al. (2011a). (a) Measured topography. (b) Time series of water level in 35 m depth offshore. 65

4.7 Comparison of deposition and erosion (D/E) curve between model results and field data. (a) Comparison between model results from MESCAPT (solid line) and Apotsos et al. (2011a) using measured profile (dashed line), and field data (grey circles). (b) Black crosses are the points picked from MESCAPT results where there are field measurements (grey circles). 67

4.8 Case setup. (a) Bathymetry is composed of an onshore section with a 1 : 100 slope and an offshore 1 : 20 slope. Green dashed-line rectangle delineates the domain where sediment transport is handled. Sediment initially forms a 0.5 m thick layer that extends from -150 m to 10 m. Dark grey area that surrounds the sediment is immobile basement. (b) Bar plot of initial grain-size distribution. Grain size is in ϕ scale. For this case, a positively-skewed distribution is used, and the coarsest fraction is 50%. (c) and (d) show right boundary conditions. Tsunami waves have a period of 200 s, and storm waves 10 s. They both have initial wave heights of 1 m. 69

LIST OF FIGURES

4.9 Storm simulation results. The top pane shows the sand bed surface elevation at end of the storm simulation. The dashed line delineates where a grain-size analysis is performed (Fig. 4.11). The bottom pane shows the deposition-erosion curve, where positive denotes deposition and negative erosion, in comparison with the original bed elevation. 70

4.10 Tsunami simulation results. The configuration is the same as Fig. 4.9. 71

4.11 Comparison of grain-size analysis plots between different sampling density for the idealized storm case. The area of interest is delineated with dashed lines in Fig. 4.9. The top pane uses a sampling density of one Δx per 2.5 m, while the bottom doubles the density. The top columns are aligned with the same column in the bottom. Each column shows the grain-size distribution and d_{50} trend of the deposition layers. The percentage of each sediment class within a layer is denoted by a color-coded rectangle. A black curve with yellow dots connecting all the layers shows the d_{50} trend. The columns are showing the thickness of the movable bed instead of the elevation. 73

4.12 Comparison of grain-size analysis plots between different sampling density for the idealized tsunami case. The area of interest is delineated with dashed lines in Fig. 4.10. The top pane uses a sampling density of one Δx per 2.5 m, while the bottom doubles the density. Refer to the caption of Fig. 4.11 for definition of colors and curves. 74

LIST OF FIGURES

A.1 Comparison between numerical simulation results and experimental data of an $h/D = 0.3$ initial solitary wave. Due to the limitations of the non-dispersive shallow water equations, the model couldn't reproduce the breaking process very well, as is shown in the wave run-up in the top two sub-plots. 99

A.2 Comparison between numerical simulation results and analytical solutions of landslide generated tsunami. Case (1). 101

A.3 Comparison between numerical simulation results and analytical solutions of landslide generated tsunami. Case (2). 102

List of Tables

4.1	Notation	79
-----	--------------------	----

Chapter 1

Introduction

According to the Intergovernmental Panel on Climate Change Fourth Assessment Report (Parry, 2007), the world's population in coastal and low-lying areas will increase to 1.8 - 5.2 billion by 2080 from the current 1.2 billion. The growth rate is staggering, almost quadrupling at the maximum estimate. In the US, more than 50 percent of the population live along the coast. The coastal area attracts people with its abundance in natural resources and tourism. However, the migration to coastal areas also creates higher risks due to the various forms of coastal hazards. Tsunami and storm are the two major events, which are more transient comparing to some other types of coastal natural hazards, such as, sea level rise. This study will focus on tsunami and storm only.

A tsunami is a series of long waves caused by earthquakes, volcanic eruptions, submarine landslides or even meteorite impacts. The tsunami waves in the deep ocean typically have

wave lengths up to hundreds of kilometers, yet with only less than 1 m wave height. This makes tsunami waves in the deep ocean difficult to detect, however, when they approach the shore, the waves can reach tens of meters high due to shoaling effect. For example, the maximum height of the tsunami was measured to be more than 30m on the west coast of northern Sumatra for the 2004 Indian Ocean Tsunami, whereas the deep ocean wave heights were less than 1 m.

While tsunamis are caused by a sudden displacement of a large volume of water from different generation mechanisms, storms are associated with disturbances of the atmosphere. For instance, a tropical cyclone is a storm driven by a low-pressure warm core where heat is released when moist air rises and condenses, causing strong winds, and heavy rain. Therefore, in addition to flooding hazard, storms also generate strong winds that can cause great damage.

Tsunamis and storms are capable of causing significant casualties and damages to infrastructures in coastal areas around the world. For tsunami and storm hazard assessment, two fundamental factors are the frequency and magnitude of each type of event (Jaffe, 2008). Since both major tsunamis and storms are relatively infrequent, especially tsunamis, it is crucial to utilize the deposit they left behind to study the past events where no written record is available. Deposits are concrete evidence that can be used to determine the magnitude of causative event. However, for locations where both tsunami and storm are able to occur, whether or not both types of deposits can be differentiated becomes an important question (Dawson and Shi, 2000).

A number of studies have been conducted specifically for comparing tsunami and storm deposit in the past decade. Nanayama et al. (2000) studied the differences between deposits from the 1959 Miyakojima typhoon and 1993 Hokkaido-nansei-oki tsunami at southwestern Hokkaido, Japan. Using a small trench 60 m landward of the shoreline, they identified that the 35 cm thick tsunami deposits contain four layers, each corresponding to the run-up and run-down of the two main waves of the tsunami. In comparison, the storm deposits have one single layer laid down by the landward flow. For the composition of the deposits, the tsunami inundation deposits are composed of mostly marine sand, and the tsunami return flow deposit are composed of non-marine sand, soil clasts, garbage, plants, and stream gravel with imbrications. In contrast, the storm deposit has exclusively foresets dipping landward, and the source of the storm sand is marine only. The only similarity between the two deposits is that they both thin inland.

Goff et al. (2004) compared the differences between the 2002 Easter storm deposit and the 15th-century Okoropunga tsunami deposit in southeastern North Island, New Zealand. The tsunami deposit fines both inland and upwards, whereas the storm deposit shows only coarsening at the inland extent. Another difference is that tsunami deposit contains a wider spectrum of grain sizes, comparing to better-sorted storm deposit. This is probably because the tsunami was able to entrain finer sediments from below the storm wave base. In addition, the basal contact of the tsunami deposit is erosional, containing rip-up clasts. In contrast, the storm basal boundary is sharp.

Tuttle et al. (2004) tried to distinguish tsunami deposits from storm deposits in eastern

North America using the 1929 Grand Banks tsunami and the 1991 Halloween storm. Key findings include that the 1929 tsunami deposits are characterized by massive or fining-upward subunits, while the 1991 storm deposits display foreset and planar stratification with channel structures. The tsunami deposits reach much higher than the storm deposits.

While the previous studies only considered two events at the same or close locations, Morton et al. (2007) attempted to identify distinguishing physical features between the two types of deposits using events of similar magnitudes, yet from different areas. With this approach, they tried to summarize the similarities and differences that are irrelevant to local variations. After detailed description of the sedimentological characteristics of the 1998 Papua New Guinea tsunami, the 2001 Peru tsunami, the 1961 Hurricane Carla, and the 2003 Hurricane Isabel at sub-regional scale, transect scale, and trench scale, the following conclusions are made. For extreme tsunami events, their deposits are able to reach beyond the maximum possible elevations of storm deposits. Tsunami deposits are usually normally graded and show massive structures. Tsunami deposits typically contain internal mud laminae or intraclasts close to the base. Offshore flow direction indicators are also diagnostic of tsunami deposits. Sandy storm deposits, in contrast, generally have numerous subhorizontal planar laminations, abrupt inland thinning trend, and may contain bed-load transport structures like foresets and climbing ripples.

One common conclusion from the aforementioned studies is that cross-beddings are exclusively attributed to storm. However, cross-beddings, characteristic of bedload transport deposition, have also been discovered in tsunami deposits. For instance, landward-dipping

foresets and parallel-laminated sand layers overlying beach sediments were found in the 2004 Indian Ocean Tsunami deposits in India (Bahlburg and Weiss, 2007); extensive bedforms with foresets dipping both landward and seaward were found in the deposits laid down by the 2004 Indian Ocean Tsunami in Thailand (Choowong et al., 2008); Nanayama and Shigeno (2006) reported current ripples in the upper two units deposited by the 1993 tsunami in southwest Hokkaido. The existence of bedload deposits does not contradict the fact that tsunamis are capable of transporting sediment in suspension, because the flow condition may vary dramatically with different tsunami magnitudes and configurations of the beach, factors including onshore slope, bed roughness, and local topography (Apotsos et al., 2012).

In addition to the physical criteria, there are many other approaches that can be employed to differentiate between tsunami and storm deposits, such as, biological, (geo-)chemical, geomorphological methods. Integration of these different proxies, could help the differentiation with more confidence (Goff et al., 2012).

Observations in the field have found that landward tsunami deposition usually does not match the inundation extent. For instance, continuous sandy sheet was deposited up to 600 m inland in the Algarve, Portugal, by the earthquake induced great Lisbon tsunami. Discontinuous sandy deposit is found farther inland, which eventually disappears. However, the tsunami inundation was observed to be much farther inland than the deposits (Hindson et al., 1996). More recently, Goto et al. (2011) found that the maximum water inundation was 4.5 km after the 2011 Japan tsunami, and that sandy sediments thicker than 0.5 cm only reach up to 2.8 km inland. Abe et al. (2012) further studied the Japan tsunami deposits

and reported that for locations where inundation is less than 2.5 km, sand reaches over 90% of the maximum local inundation. For inundations larger than 2.5 km, sand could be traced up to 50% to 76% of the inundation. These field observations motivated my first research project (Chapter 2). In our study, we explored the relationship between the inland reach of sand and the maximum inundation of tsunamis, in order to better interpret paleo-tsunami deposit where no historical record is available. We carried out a parameter study with the well-known MOST model was coupled with a simple deposition model. The sediment model calculates the shear velocity and compare it with the critical shear velocity, and marks the farthest inland location where there is deposition. After a tsunami retreats, the maximum inland extent of sand is found. This process is repeated for a number of different initial wave height, onshore slope and grain sizes. Finally, we defined the deposition ratio as the distance of the sediment extent over the water inundation distance, and established the quantitative relationship between the deposition ratio and the three varying parameters.

A number of small projects were conducted after the study on the relationship between the sediment and inundation limit of tsunamis. The model SeTuPS was developed for a sedimentology group led by Dr. Bahlburg in the University of Münster. SeTuPS stands for Settling Tube Python scripts, which is used to process settling tube data of time versus weight into grain-size distribution. Instead of using a constant settling velocity, SeTuPS calculates the detailed movement of the sediments, which includes both the initial acceleration and the final constant settling stage. For a specific settling tube, the settling time of a range of grain sizes (in ϕ scale) are calculated with SeTuPS, and then the relationship between

grain size and settling time can be established. This relationship is then used to convert the time data taken from the settling tube to grain size. SeTuPS has been constantly updated with the need for better user interface, the ability to handle a range of file types, cross-platform (Windows and Linux), and batch processing, and has now become a scientifically robust, flexible and user-friendly software. We intend to publish the software in the journal *Computers and Geosciences*.

The SeTuPS later evolved into a one dimensional vertical (1DV) settling model in which we assume that the sandy sediments of different grain sizes are initially suspended and evenly distributed on the top of the water column. Instead of modeling individual sediment grains, we assume that a small group of sediment of the same size move together, in order to reduce the computation time. Since this is a one dimensional model, each sediment group is assigned a thickness. The settling process is modeled as is in the SeTuPS. When sediment groups deposit, they are stacked closely based on the order of deposition. This model was used to qualitatively visualize the vertical grain-size trend, and how the trend is related to the settling height and initial grain-size distribution. The 1DV model further evolved into a two dimensional vertical (2DV) model, where the hydrodynamics is modeled with linear wave theory. However, since no inundation is modeled, only offshore sediment dynamics were studied.

Another project is a US Army Corp of Engineers (USACE) project, titled “The Role of Shoreline and Bottom Type Dynamics in Understanding Barrier Island Vulnerability and Resiliency”. This is a collaborative project with the research group led by Dr. Jennifer L.

Irish from the department of Civil & Environmental Engineering, Virginia Tech. The goal of this project is to understand the influence of bottom types and vegetation on morphological changes of barrier islands during storms. The two study locations, Moriches Inlet, NY and Assateague Island, VA, were chosen based on topographic features, data availability and meeting the U.S. Army Corps of Engineers mission to protect coastal infrastructure and promote healthy ecosystems. The numerical model, XBeach, is used to simulate hydrodynamics and sediment transport (Roelvink et al., 2009). For the first stage, we base our simulations on idealized uniform longshore beach profiles and sediment properties. The representative beach profiles are created using lidar data from JALBTCX (The Joint Airborne Lidar Bathymetry Technical Center of Expertise) for topography and ETOPO¹ data for bathymetry. The sediment at the barrier island is divided into two layers. The surface layer is vegetated, which is achieved by applying mobility restriction to (i.e., reducing the equilibrium concentration of) the sediment class of this layer. Beneath the surface layer is normal beach sand. A parameter study is carried out in which we vary the beach profile and the mobility reduction factor. Specifically, we aim to quantify how the barrier island profile and the intensity of vegetation affect the possibility of breaching and the amount of erosion. The second stage will involve non-uniform longshore profiles and sediment properties. Realistic profiles and bottom types will be used to investigate the conditions that lead to the breaching in Moriches Inlet and Assateague Island during Hurricane Sandy. The first stage of this project will be finished soon and we anticipate to publish the results in the near

¹ETOPO is a global relief model of Earth's surface that integrates land topography and ocean bathymetry.

For example, ETOPO1 is an ETOPO model with 1 arc-minute resolution.

future.

The particle-like approach in the SeTuPS and its two derivatives demonstrated the advantages of the particle approach, that is, detailed particle motion can be obtained and hence the source and sink of particles are easily traced. Also, the deposition pattern can be kept in high resolution. Besides, from the USACE, I understood that although traditional concentration-based sediment transport model is efficient, it lacks of the capability of the particle models mentioned above. Moreover, the shallow water hydrodynamic model used in XBeach is efficient to model wave run-up. Therefore, the idea of couple a shallow water hydrodynamic model and the particle based sediment transport model is born, with the purpose to study the similarities and differences between tsunami and storm sediment transport and deposits. The MEso-SCALE Particle Transport (MESCAPT) model was developed and is still being constantly improved in terms of functionalities and computational efficiency. The MESCAPT model combines the advantages of concentration-based models and particle-based models, where the former is efficiency and the latter is that detailed transport and deposit information can be obtained. Another advantage of particle model is that bed-load and suspended-load sediment transport do not require different set of equations as is employed in concentration based models. This is especially important for situations where the shear stress fluctuates quickly and with significant magnitude changes that constantly change the transport mode back and forth between bed and suspended-load. The idea of using a group of sediment grains is defined in MESCAPT as a meso-scale particle. The meso-scale concept assumes that a small number of sediment grains have the same properties and do not

change during transport. The MESCAPT model has been validated against field data, and is able to reproduce macroscopic morphological changes and microscopic grain-size trends during storms and tsunamis. Details of the MESCAPT model is shown in Chapter 3.

Chapter 2

On sediment extent and runup of tsunami waves

Abstract

Tsunami sediments play an important role in tsunami hazard assessments. Recent tsunami events and their associated tsunami deposits have produced a wealth of sediment data. Surveys of recent tsunami events observed that maximum inland tsunami inundation exceeds the maximum inland extent of sand deposition. A driving question of tsunami sedimentology is whether the difference between maximum tsunami inundation and inland extent of sand can be employed as a measure of inundation for past events for which only the extent of the sand is known. Attempts to infer the causative flow characteristics from these sediments

Published on Earth and Planetary Science Letters, 15 Jan 2013

often suffer from uncertainties in the data and from restrictive assumptions made in inversion models. The latter demonstrates that the interaction between the tsunami flow and the movable bed is not fully understood. In our contribution, we employ numerical simulations of tsunami propagation and inundation with MOST and a simple model for deposition. In our simulations, we vary the onshore slope, the initial amplitude, which can be interpreted as offshore wave amplitude, and the grain size. While the initial amplitude and onshore slope influence the difference between maximum inundation and sand extent, the grain size has little effect. The link between the onshore slope, initial amplitude and the difference between the maximum tsunami inundation and inland sediment extent can be employed as a first-order quantitative tool to estimate tsunami flow characteristics and maximum inundation from tsunami deposits. We anticipate these results will improve tsunami hazard assessments and narrow the gap between field observations and numerical simulations.

2.1 Introduction

Since the 2004 Sumatra event, tsunamis have received increased public and scientific attention. A wealth of quantitative data has been collected since then, i.e. for the 2007 Bengkulu, 2008 Tonga, 2009 Samoa, 2010 Chile and 2011 Tohoku-oki tsunami events. Quantitative data gathered after each of these events can include flow depth and runup measurements to characterize the tsunami flooding, as well as measurements, description and sampling of sedimentary effects, either manifested as erosion or deposits. Quantitative characteristics of

the flooding zone play a crucial role in the continuing effort to validate computer models and to inform educational efforts to increase tsunami awareness and preparedness. Emphasis is also placed on quantitative sedimentary data as the geologic record of tsunamis has become more and more important for tsunami hazard assessments (Huntington et al., 2007). With the help of tsunami deposits, the recurrence intervals of tsunamis in a given region can be inferred, such as in Jankaew et al. (2008) for Phra Thong Island (Thailand) where different sand layers were ascribed to tsunamis. There has been success in inferring hydrodynamic characteristics of the tsunami that result in sediment deposition (Jaffe and Gelfenbaum, 2007; Spiske et al., 2008; Witter et al., 2011). However, a more general physical understanding of hydrodynamic processes and their interplay with sediment still is in an early stage of development.

Tsunami deposits undoubtedly are the recordings of past events (Huntington et al., 2007, and references therein). It is possible to draw simple conclusions from the spatial distribution of tsunami deposits, e.g. the tsunami must have reached at least to the point where the sandy tsunami deposits end. Two examples where this condition is employed come from Martin et al. (2008) and MacInnes et al. (2010). Martin et al. (2008) uses the alongshore distribution of tsunami sediments on the west coast of Kamchatka to untangle tsunami deposits from two earthquakes that took place in 1969 and 1971. MacInnes et al. (2010) employs the longshore distribution of tsunami deposits ascribed by the 1952 tsunami on Kamchatka to infer an ensemble of possible rupture characteristics of the parent 1952 M 9.0 Kamchatka earthquake (Kanamori, 1977).

Along the Japanese coast in the vicinity of Sendai, tsunami deposits, determined to have been formed by the 869 AD Jogan tsunami (Minoura and Nakaya, 1991; Minoura et al., 2001; Sugawara et al., 2011), were employed to infer the magnitude of the parent earthquake. Satake et al. (2008), Namegaya et al. (2010) and Sugawara et al. (2011) estimated a magnitude of about 8.4. In hindsight, after the March 11, 2011 Tohoku-oki earthquake and tsunami, this magnitude estimate is considered flawed. Yet, it should be noted that the estimated magnitude was state-of-the-art at the time and that the research resulting from the inference was scientifically sound and published in peer-reviewed journals. However, the changed interpretation of the Jogan earthquake and tsunami also demonstrates that the apparent gap between paleotsunami geology and computer-based simulations ought to be narrowed in order to avoid future surprises like the March 11, 2011 event.

Tsunami sediments have been a research focus for more than two decades. However, it is still not straightforward to identify tsunami deposits in the geologic record, not to mention the difficulties that exist for inferences of flow characteristics from the deposits. Attempts to characterize tsunami deposits from a more general point of view have been made (Nanayama et al., 2000; Goff et al., 2004; Bourgeois, 2009; Goff et al., 2012), but are not always successful due to the diversity of observed sedimentological features. The variety of different sediment characteristics is a reflection of hydrodynamic variability and sediment transport conditions during tsunami inundation. It has often been noted that tsunami sediments, mostly of sandy and silty grain sizes, do not extend to the maximum inundation, e.g. Bourgeois (2009, and references therein) and Goff et al. (2012, and references therein). Most recently,

Goto et al. (2011) reported for the March 11, 2011 Tohoku-oki tsunami that the maximum inundation was 4.5 km and that the sandy sediments could only be traced up to 2.8 km (sand layer >0.5 cm) on the Sendai plain. Abe et al. (2012) refined this observation for the Tohoku-oki tsunami and noted that for inundations less than 2.5 km, sand (sand layer >0.5 cm) reaches commonly to over 90 % of the maximum local inundation distance. For inundations larger than 2.5 km, sand (sand layer >0.5 cm) could be traced up to 50 % to 76 % of the maximum local inundation distance. Furthermore, post-depositional changes of tsunami sediments can occur, as is reported from Thailand after the 2004 Indian Ocean tsunami by Szczucinski (2012), which render inferences of the causative flow conditions even more difficult. The processes that change the characteristics of tsunami sediments can work quickly and effectively, and can start shortly after the event. For example, on the open rice paddy fields in the vicinity of the Sendai Airport, Goto et al. (2011) observed an up to 1-cm thick top layer of the tsunami deposits that was reworked by wind only weeks after the March 2011 Tohoku-oki tsunami. However, Bondevik (2008) and Atwater et al. (2012) demonstrate for swales between beach ridges and hyper-saline lakes that tsunami deposits can be sheltered almost completely from destructive post-depositional processes.

In this contribution, we consider the question: Can the maximum inland extent of tsunami deposits be utilized to infer the maximum inundation or runup of a tsunami? To answer this question and to evaluate if it is possible to develop an analytical tool to infer the maximum inundation and runup from the sediment extent, we employ numerical modeling of tsunami evolution (propagation and inundation) with the well-known MOST code (Titov

and Synolakis, 1995; Titov and Synolakis, 1998) and use a threshold model for deposition. For simplicity, we use a bathymetry close to the canonical problem for shallow-water waves with a constant depth part and a sloping beach to the shoreline. Because we consider only deposition on land, we vary the slope of the dry beach. For initial water surface conditions, we employ solitary waves from Synolakis (1986, 1987), who derived the long-sought analytical solution of the shallow-water problem.

2.2 Theoretical Background and Model Setup

2.2.1 The MOST code

For the propagation and inundation of tsunami waves, we employ the MOST code (Titov and Synolakis, 1995; Titov and Synolakis, 1998). MOST solves the shallow-water equations with a splitting technique that is similar to the method of characteristics. The benefit of the numerical scheme is that the wave elevation and depth-averaged velocities are efficiently computed. Furthermore, the MOST code is the standard code for simulating tsunami propagation and inundation dynamics at NOAA's Center for Tsunami Research. MOST has been employed for real-time forecasting (i.e., Wei et al., 2008), and MOST is verified and validated with analytical solutions of the shallow-water theory experiments presented in Synolakis (1986, 1987). Furthermore, MOST was also the first code that was certified with NOAA's standard and procedures for tsunami inundation codes (Synolakis et al., 2008). For

simplicity, we employ a one-dimensional version of MOST (MOST-1D).

2.2.2 Sediment Model

We implemented a simplified sediment deposition model into MOST. It should be noted that the implemented model does not simulate sediment erosion and transport. To simulate sediment erosion, transport and deposition, an advection-diffusion equation for the distribution of suspended sediment must be numerically solved along with an equation to compute bed-load fluxes and an Exner-type equation to update the elevation of the sediment surface. A model simulating sediment dynamics is desirable, but it also would require a comprehensive validation study. Important data gathered in a controlled environment do not exist for such a validation. Furthermore, we assume an infinite supply of all grain sizes.

We argue that a deposition model using the shear stress u^* generated by the flow and a critical shear stress u_{cr}^* for a grain of size d_ϕ can be employed to estimate deposition. The two conditions for deposition are: (1) $u_t^* < 0$ and (2) $u^* < u_{cr}^*$ where u_t^* is the first temporal derivative of the shear velocity u^* and u_{cr}^* is the critical shear velocity for d_ϕ from the Shields diagram. We employ a depth-averaged law of the wall:

$$u_* = \bar{u}\kappa \frac{\eta - z_o}{z_o - \eta + \eta \log(\eta/z_o)} \quad (2.1)$$

to compute the shear velocity u^* from the depth-averaged flow velocity \bar{u} from MOST. In equation (2.1), κ denotes the van Karman's constant (≈ 0.41) and η is the flow depth computed with MOST-1D. The parameter z_o is the reference height above the wall, for which

we assume Nikuradse’s roughness length, $z_{NK} = d_\phi/30 = z_0$.

The critical shear velocity, u_{cr}^* ($= f(d_\phi)$) is computed from the discretization of the Shields diagram:

$$Y_{cr} = k_1 X_{cr}^{k_2} + k_3 \exp [k_4 X_{cr}^{k_5}] \quad (2.2)$$

from Weiss (2008). The coefficients are: $k_1 = 0.15$, $k_2 = -1$, $k_3 = 0.05$, $k_4 = -8.0$, and $k_5 = -0.9$. For scaling of X_{cr} and Y_{cr} we use $X_{cr} = (u_{cr}^* d_\phi) \nu^{-1}$ and $Y_{cr} = (\rho u_{cr}^*) (d_\phi \gamma)^{-1}$.

The latter is rearranged to compute u_{cr}^* in an iterative procedure. We argue that the Shields diagram is appropriate to infer u_{cr}^* because of its simplicity. More complicated methods to estimate u_{cr}^* require approximations for additional parameters, such as roughness and grain-size distribution. The quantification of roughness, for example, generated by hopping grains in the bed-load layer (Wiberg and Smith, 1985, 1989) or by bed forms, requires detailed knowledge of the pre-transport grain-size distribution, volume of grain sizes available for transport, and bed conditions.

The shear stress, exerted by the flow, is compared to the critical shear stress for different grain sizes. Applying the two conditions defined above for deposition, we can infer whether sediment grains of a certain size remain in the flow or are deposited. These calculations take place individually for each grain size at each time step and at each point along the dry part of the sloping beach. This simple threshold model is added to MOST-1D. Information from the hydrodynamic model is passed to the deposition model. However, information from the deposition model is not returned to the MOST hydrodynamic model.

2.2.3 Model Setup

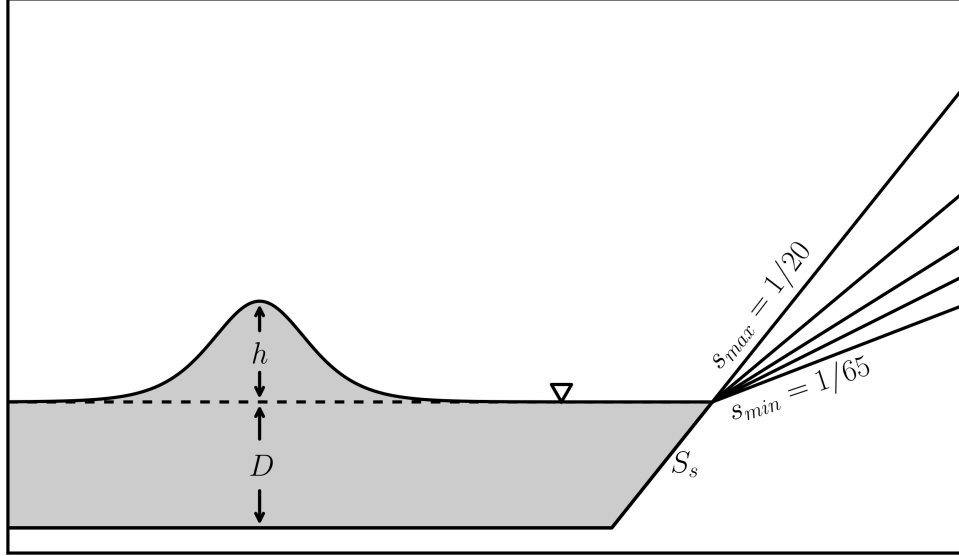


Figure 2.1: A sketch of the bathymetry and solitary wave for the MOST-1D tsunami simulations. The gray region shows the sea water covering the constant depth and sloping beach. Various dry slopes are connected to the right edge of shelf. The initial sea level is set at the conjunction of shelf and beach. h is solitary wave height, D is constant water depth, $s = \cot(\beta)$ is the beach slope where β is the angle of the beach, and $S_s = \cot(\beta_s)$ is shelf slope. Note that this figure is not plotted to scale.

Our parameter study is based on a bathymetry that features a constant deep-water depth D and a constant sloping beach to the shoreline S_s . The geometric setup is depicted in Fig. 2.1. We employ solitary waves from Synolakis (1987) for the initial water surface $\eta(x, t = 0)$:

$$\eta(x, t = 0) = h \operatorname{sech} \left[\sqrt{\frac{3h}{4D^3}} (x - X_1) \right], \quad (2.3)$$

in which h is the amplitude of the solitary wave, X_1 represents the x location where $\eta(x, t =$

$0) = h$. The location X_1 is kept constant in our simulation. Furthermore, the dry part of the sloping beach is denoted by s , which is a variable in our parameter study and varies from $s_{max} = 1/20$ to $s_{min} = 1/65$. The grain-size spectrum is defined from $d_\phi = 4$ (0.0063 mm) to $d_\phi = -1$ (2.0000 mm), representing sand.

The parameter space in our study is three dimensional with a varying initial solitary wave amplitude h , varying dry beach slope s , and varying grain size d_ϕ . For this study, we use 18 different initial wave amplitudes, ten different slopes and six different grain sizes. Thus, the total number of simulations is 1080. It should also be noted that we normalize the slope to $\tilde{s} = s S_s^{-1}$ and the initial wave amplitude to $\tilde{h} = h D^{-1}$. The grain size is not normalized. We will demonstrate later that the grain size has very little effect on the results. For the data analysis, we employ the normalized parameters for slope (\tilde{s}) and initial wave amplitude (\tilde{h}). In each simulation, we detect the maximum inundation distance and the maximum inland reach of each grain size. To compare the two extents, we define a deposition ratio ξ with

$$\xi = \frac{\epsilon_\phi}{\iota} \quad (2.4)$$

The parameter ι denotes the maximum inundation for different initial wave amplitudes and dry beach slopes, and ϵ_ϕ are the respective inland extents of different grain sizes.

2.3 Results

Intuitively, the deposition ratio is a function of the initial wave amplitude \tilde{h} , slope \tilde{s} , and grain size d_ϕ . Figure (2.2a) depicts the deposition ratio as a function of initial wave amplitude.

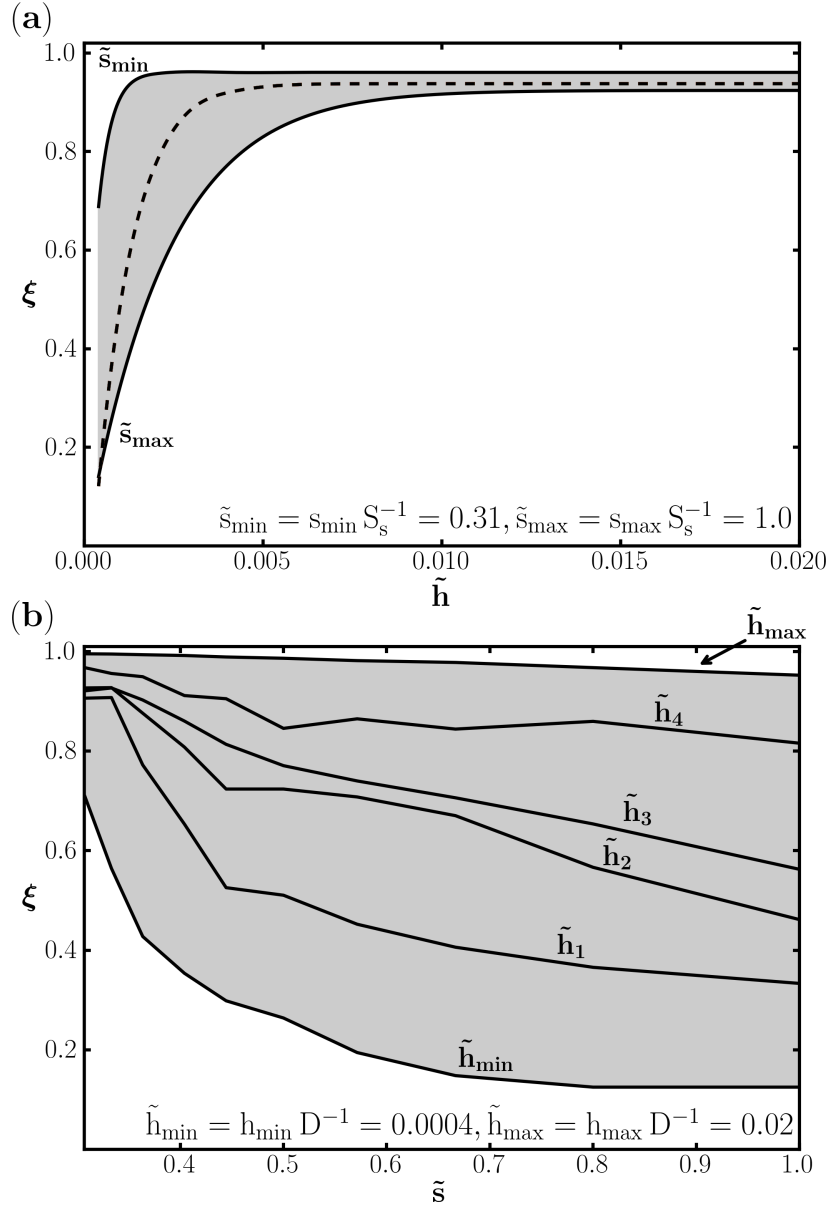


Figure 2.2: Deposition ratio versus normalized beach slope $\tilde{s} = s S_s^{-1}$ and normalized initial wave height $\tilde{h} = h D^{-1}$. (a) shows an envelope where smoothed deposition ratio data at \tilde{s}_{min} and \tilde{s}_{max} define the upper and lower boundaries respectively. (b) shows again an envelope of deposition ratio, except that \tilde{s} is on the x-axis and \tilde{h}_{min} and \tilde{h}_{max} define the boundaries.

For shallow slopes, the deposition ratio reaches a maximum ($\xi \approx 1$) in a very small interval of increasing \tilde{h} (saturation at $\tilde{s} = 0.0025$), and for steeper slopes this interval is wider (saturation at $\tilde{s} = 0.010$). The dashed line in this figure represents a slope of 1/30. It turns out that all grain sizes overlay each other perfectly for the slope of 1/30. This also holds true for all other slopes within the envelope defined by \tilde{s}_{min} and \tilde{s}_{max} . It should be noted that Fig. 2.2a exhibits a fit to the data with:

$$\xi(\tilde{h}) = l_1 + l_2 \exp \left[-(l_3 \tilde{h} - l_4)^2 \right] \quad (2.5)$$

where l_1 , l_2 , l_3 , and l_4 are fitted coefficients. The plot of ξ vs. \tilde{s} (Fig. 2.2b) shows that for larger initial wave amplitudes \tilde{h} , the deposition ratio change little and remains very close to $\xi \approx 1$ for all slopes. However for smaller \tilde{h} , for example $\tilde{h} = \tilde{h}_{min}$, the deposition ratio evolves from $\xi = 0.1$ for $\tilde{s} = 1$ to $\xi = 0.6$ for $\tilde{s} = 0.33$. Fig. (2.2b) also shows that deposition ratios for different grain sizes overlay each other for $\xi = f(\tilde{s})$ for the initial wave amplitudes \tilde{h}_1 through \tilde{h}_4 . For all grain sizes, a maximum Root Mean Square Error of $RMSE_{max} = 0.0859$ of deposition ratios to their mean value indicates that the grain size has little influence on the deposition ratio and can therefore be neglected. The parameter space is reduced to two dimensions, initial wave amplitude \tilde{h} and slope \tilde{s} .

With a two-dimensional parameter space, we can create a surface representing the deposition ratio that depends on the initial wave amplitude and the slope. The function to represent this surface $\xi = f(\tilde{s}, \tilde{h})$ is:

$$\xi(\tilde{s}, \tilde{h}) = m_1 + m_2 \exp [m_3 \tilde{h} \tilde{s}^{-1}] + m_4 \exp [-(m_5 \tilde{h})^2] \quad (2.6)$$

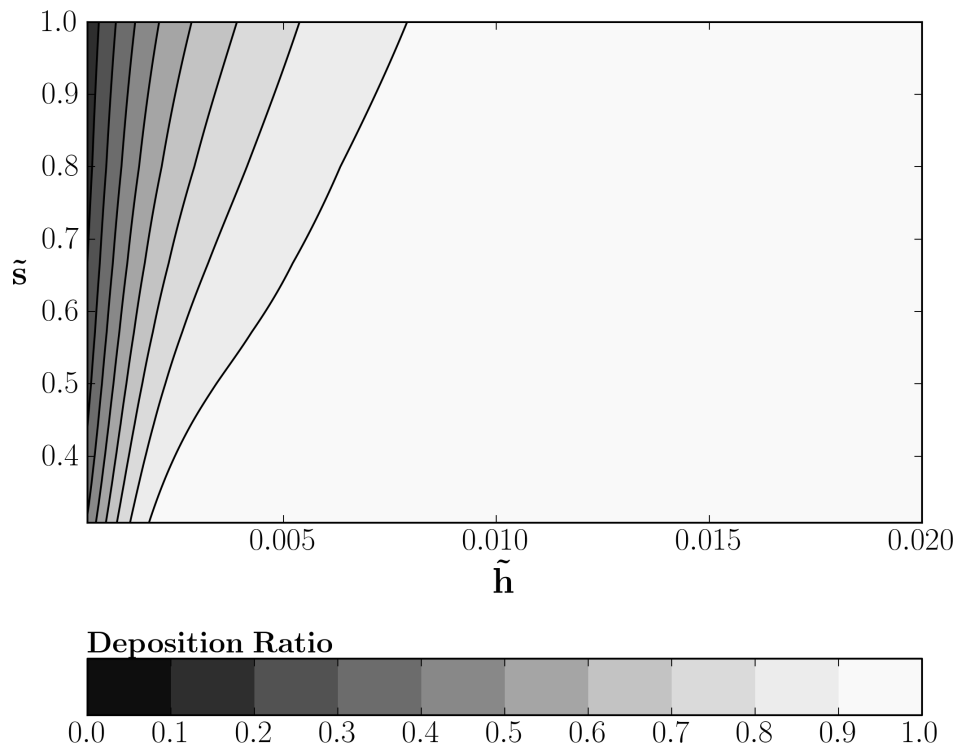


Figure 2.3: Contour plot showing deposition ratio as a function of normalized beach slope \tilde{s} and initial wave height \tilde{h} . The equation is described in Eq. (2.6). This two dimensional plot better illustrates the tendency of deposition ratio saturation interval to increase as slope becomes steeper. Most of the parameter space exhibits a deposition ratio of $\xi > 0.9$, indicating sediment extents commonly approximates tsunami inundation.

where m_1 , m_2 , m_3 , m_4 , and m_5 are fitted coefficients. A good quality the fit is indicated by an $R^2 = 0.9600$ and a Root Mean Square Error of $RMSE = 0.0511$. The contour plot of the deposition ratio ξ from Eq. (2.6) is given in Fig. (2.3). For small slopes \tilde{s} the increase from a small to a large deposition ratio takes place over much narrower band of initial wave amplitudes than for larger values of \tilde{s} . As a reminder, small values of \tilde{s} refer to gentle slopes and large values of \tilde{s} denote steeper slopes. It should also be noted that 82% of the parameter

space exhibit a deposition ratio of $\xi > 0.9$.

2.4 Discussion and Conclusions

In this contribution, we carried out a parameter study to explore the influence of the initial wave amplitude, which can also be considered as the offshore wave amplitude, the onshore slope, and grain size. Our analysis revealed that for sand the grain size has little effect on the deposition ratio. We ascribe this outcome to a relatively large velocity of the overland flow and the dynamics of the tsunami front, which decelerates quickly near the point of maximum inundation. This finding also is a blessing in disguise because possible inferences of the maximum inundation and runup employing the deposition ratio, do not depend on the grain size distribution. In this regard, Szczucinski (2012) demonstrated that tsunami sediments can be altered by post-depositional processes. For example, Goto et al. (2011) observed that the top of Tohoku-oki tsunami deposit was reworked by wind. Furthermore, bioturbation (flora and fauna), and human activity can mix or completely destroy tsunami deposits. Not all natural post-depositional processes are active in a given sedimentary environment. Therefore, the effectiveness of post-depositional changes depends very much on the characteristics of sedimentary environment.

The initial or offshore wave amplitude and the onshore slope influence the deposition ratio (see Fig. 2.2). The deposition ratio reaches its maximum sooner for smaller slopes than for steeper ones. Furthermore, for large initial wave amplitudes, the deposition ratio is close

to one for all slopes. However, the deposition ratio decreases significantly for increasingly steeper slopes and lower initial wave amplitudes. Therefore, we argue that the deposition ratio as a function of the offshore wave amplitude and onshore slope can be applied in studies of ancient tsunami deposits. We suggest to employ Fig. (2.3) and propose the following scenario to apply our findings. For this demonstration, we assume that we successfully mapped the inland extent of a tsunami deposit in a certain area. For the paleo onshore slope, we assume that it is very similar to the modern one. The difficulty is, however, to estimate the offshore wave amplitude because the offshore wave amplitude is linked to the location, tsunamigenic processes (e.g. earthquake, landslide, meteorite impact) and their magnitudes. For situations where the slope is small and the anticipated offshore wave amplitude is large, a deposition ratio of one can be assumed, which means that the longshore distribution of the inland-deposit extent also represents the maximum inundation and runup. However, the deposition ratio requires adjustment for smaller offshore wave amplitudes and steeper slopes. To produce a suite of different potential magnitudes and locations of the tsunamigenic events, an iterative framework is needed.

As a reminder, Abe et al. (2012) reported that for sand layers thicker than 0.5 cm, the deposition ratio is between 0.57 and 0.76 for local inundations larger than 2.5 km. For local inundations less than 2.5 km, the deposition ratio exceeds 0.9 (Abe et al., 2012). Goto et al. (2011) observed a similar deposition ratio for sand layers thicker than 0.5 cm. However, data from Goto et al. (2011) and Abe et al. (2012) suggest that sand was transported farther inland, and that tsunami deposits evolve from pure sand to sand-dominated to mud-

dominated. For example, taking the data in Abe et al. (2012) and ignoring the thickness requirement, we can estimate that the deposition ratio increases to about 0.96 in most of the cases where the tsunami inundation was larger than 2.5 km, which is consistent with our results in Fig. (2.3). Therefore, we can state that the flow is capable of carrying sand grains in the vicinity of the inundation limit. Based on the observations by Goto et al. (2011) and Abe et al. (2012), our modeling suggests that the volume of sand was very finite and erosion of significant amounts of sediment during the overland flow did not occur. This interpretation is supported by the observations by Goto et al. (2011) and Abe et al. (2012) that for a maximum inundation of $\iota < 2.5km$ sand forming layer reached close to the maximum inundation, and for $\iota > 2.5km$ it did not. Computer simulations for a case where the volume of available sediment is lower than the flow capacity was carried out by Apotsos et al. (2011b) for the 2009 Samoa Tsunami in American Samoa. The conclusion of the limited sediment volume for the March 11, 2011 Tohoku-oki tsunami and simulations for the 2009 Samoa tsunami by Apotsos et al. (2011b) demonstrate that more comprehensive simulations of the sediment dynamics, taking the unique hydrodynamic characteristics of tsunamis and the local offshore inventory of sediments into account, are needed to better understand what information from the sedimentary environment and of the tsunami characteristics is recorded in the deposits.

We anticipate that the application of the deposition ratio will improve tsunami hazard assessments by providing a geophysically more realistic inundation limit than the cases where only the inland extent of tsunami sediment is taken into account. The limitations of our

model are the assumptions of unlimited sediment supply and that only sediment deposition is considered. However, we argue that the concept of a deposition ratio, which is quantified in Fig. (2.3), can be used as a first-order estimate of the maximum inundation of a tsunami from its deposits. By narrowing the gap between numerical modeling and field studies, we aim to eventually decipher all possible information from the tsunami deposits.

Acknowledgement

We would like to thank Breanyn MacInnes from Hokkaido University (soon Central Washington University) and Jennifer L. Irish (Virginia Tech) for their comments on earlier versions of the manuscript. Furthermore, we express our gratitude to Adam Switzer (Nanyang Technological University) and Kazuhisa Goto (Tohoku University) for their thoughtful reviews of our manuscript. This study was partially supported by the U.S.A. National Science Foundation grant NSF-EAR-1201428.

Chapter 3

The Role of shoreline and bottom type dynamics in understanding barrier island vulnerability and resiliency

3.1 Introduction

Barrier islands are long and narrow sandy deposits that run parallel to the coastline. Barrier islands serve as buffers between the open coast and the mainland, and therefore they are

A U.S. Army Corp of Engineers project.

the first line of defense that protect the coastal communities from being damaged by storm waves and surge. Under extreme conditions, barrier islands can be breached or overwashed. Breaching has many negative effects on the coastal environment and coastal communities, for example, it can result in reduction or loss of protective dunes, loss of habitat, exposure of the bay to ocean waves and currents, and increase in water level and salinity (Kraus and Wamsley, 2003). Therefore it is of vital importance to understand barrier island dynamics, including morphological evolution and flow interaction with the barrier island, as it helps advance our knowledge of barrier island vulnerability and quantify measures that increase resiliency of the coastal communities. For this study, we aim to investigate the influence of bottom types on sediment erosion, transport and deposition, and shoreline change with computational models.

3.2 Hurricane Sandy and study locations

We chose to focus on Hurricane Sandy due to the availability of high-density data and its recent impact on the U.S. coastlines. Hurricane Sandy made landfall near Atlantic City, NJ on October 29, 2012. Due to its unusually large size, the storm surge caused devastating damages in New Jersey and New York, resulting in 72 deaths and costing over \$50 billion in the U. S. Several barrier island breaches and overwash fans occurred along coastlines from the Outer Banks, NC to Long Island, NY.

For this study, two study locations are chosen. Moriches Bay is located on Long Island, NY

and was breached on the east side of the inlet during Hurricane Sandy. This location has been known to breach from the bay to the ocean during past storms, which eventually closes naturally. The area consists of sandy beaches with interspersed vegetation, which provides an ideal location to investigate the impact of bottom type on sediment erosion and deposition. Similarly, Assateague Island, VA is also characterized by a vegetated sandy seabed and was breached during Hurricane Sandy.

3.3 Simulations

Using data collected from the Joint Airborne Lidar Bathymetry Technical Center of Expertise, numerical model bathymetry grids, sediment layers and vegetation factor grids have been developed. The numerical model, XBeach, is used to simulate hydrodynamics and sediment transport (Roelvink et al., 2009). XBeach was developed to model morphological changes of complex topography during storm events, and it has shown significant skill and accuracy (McCall et al., 2010; Van Dongeren et al., 2013).

For the first stage, we base our simulations on idealized longshore uniform beach profiles and sediment properties. The representative beach profiles are created by combining lidar data from JALBTCX for topography and ETOPO data for bathymetry. The sediment at the barrier island is divided into two layers. The surface layer is vegetated, which is achieved by applying mobility restriction to (i.e., reducing the equilibrium concentration of) the sediment class of this layer. Beneath the surface layer is normal beach sand. A parameter study is

carried out in which we vary the beach profile and the mobility reduction factor. Specifically, we aim to quantify how the barrier island profile and the intensity of vegetation affect the possibility of breaching and the amount of erosion. The next stage will involve non-uniform longshore profiles and sediment properties. Realistic profiles and bottom types will be used to investigate the conditions that lead to the breaching in Moriches Inlet and Assateague Island during Hurricane Sandy.

3.3.1 Computational grid

The computational grids are created based on the Moriches Bay area. Ten cross-shore lines were used to obtain the lidar and etopo profiles. Fig. 3.1 shows the lidar profile locations. Lidar profile lines are marked by the red dots and dashed lines, and etopo profiles by the blue ones.

Fig. 3.2 shows the lidar profiles obtained from the red lines. The lidar topography displays huge variability across the shoreline. For example, the dune height ranges from 4 m to 8 m, approximately, and the berm width ranges from 50 m to 150 m. And the total barrier island width ranges from 100 m to 600 m.

For our simulations, we assume that the barrier island profile follows a simple configuration, which is comprised of a back bay, back barrier, back of dune, front of dune, berm, and shelf, as is shown from left to right in Fig. 3.3.

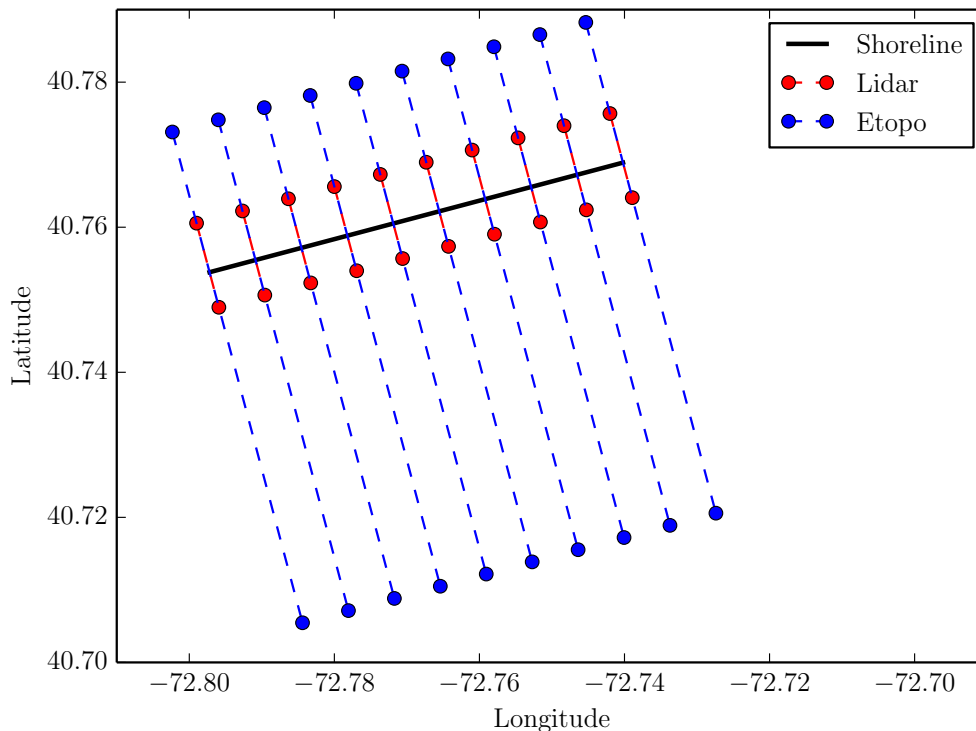


Figure 3.1: Lidar and etopo profile lines in the Moriches Bay area.

3.3.2 Vegetation layer setup in XBeach

For all the simulations, we set up ten layers and two sediment classes everywhere in the computational domain. We assume that the dune is covered by a single grass layer, which is occupied by 100% sediment class #2, and everywhere else is #1. This configuration is illustrated in Fig. 3.4. The two sediment classes have the same grain size, however, the vegetation layer is simulated by assigning a different ‘sedcal’ parameter to sediment class #2. The ‘sedcal’ parameter in XBeach directly scales the equilibrium concentration, which controls the sediment pickup capability. Therefore, a lower ‘sedcal’ value will result in less sediment being picked up, which mimics the behavior of vegetated sediments.

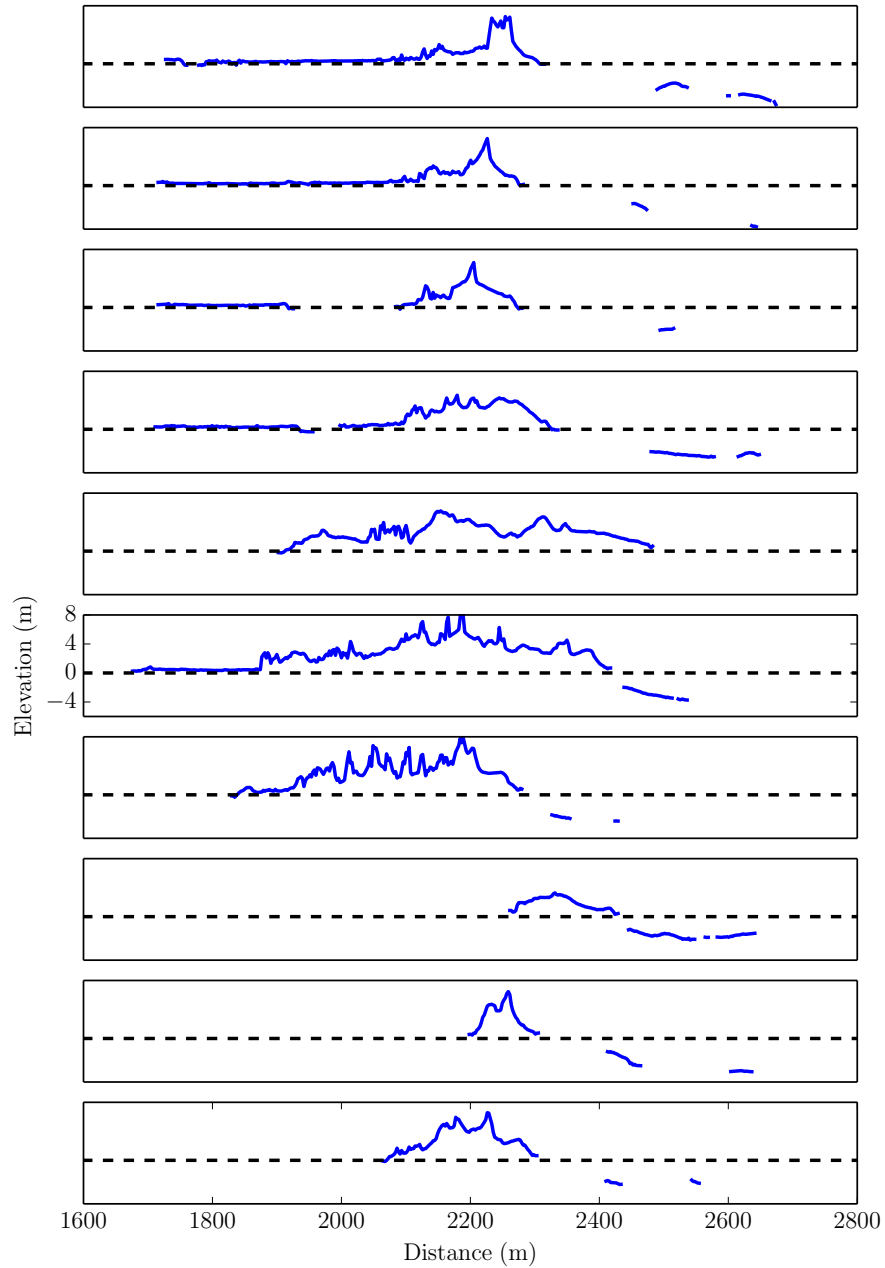


Figure 3.2: Lidar profiles of the Moriches area.

3.3.3 Model setup

For the initial set of simulations, we vary the berm width and sedcal only. Sedcal takes the following values, 0.0, 0.001, 0.01, 0.1, 0.15, 0.20, 0.25, 0.50, 0.75, 1.00, and berm width, 50,

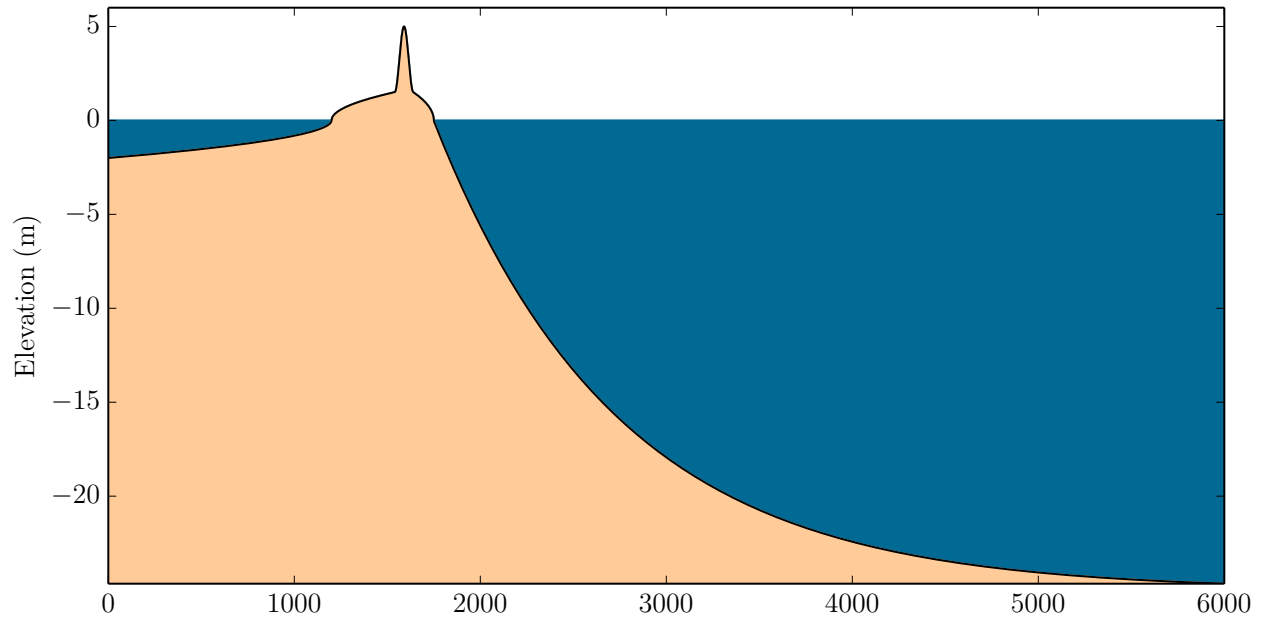


Figure 3.3: Idealized combined profile of the Moriches Bay area.

65, 75, 90, 100, 110, 125, 150 m. The other parameters are all fixed. The two sediment classes both have 0.2 mm grain size, except that class #2 has a lower sedcal value. The dune is 5 m high and 100 m wide. The significant storm wave height is 8 m, and storm surge increases from 1.0 m to 1.5 m then back to 1.0 m following the sine curve in Fig. 3.5.

3.3.4 Simulation results

Fig. 3.6 through Fig. 3.10 plots the final bed profile for each sedcal value for 5 berm widths (50 m, 75 m, 100 m, 125 m and 150 m), respectively.

In Fig. 3.6, a general trend is that as sedcal increases toward 1.00, the amount of dune erosion becomes larger. For 0.00 and 0.001, there is very little erosion. As sedcal increases

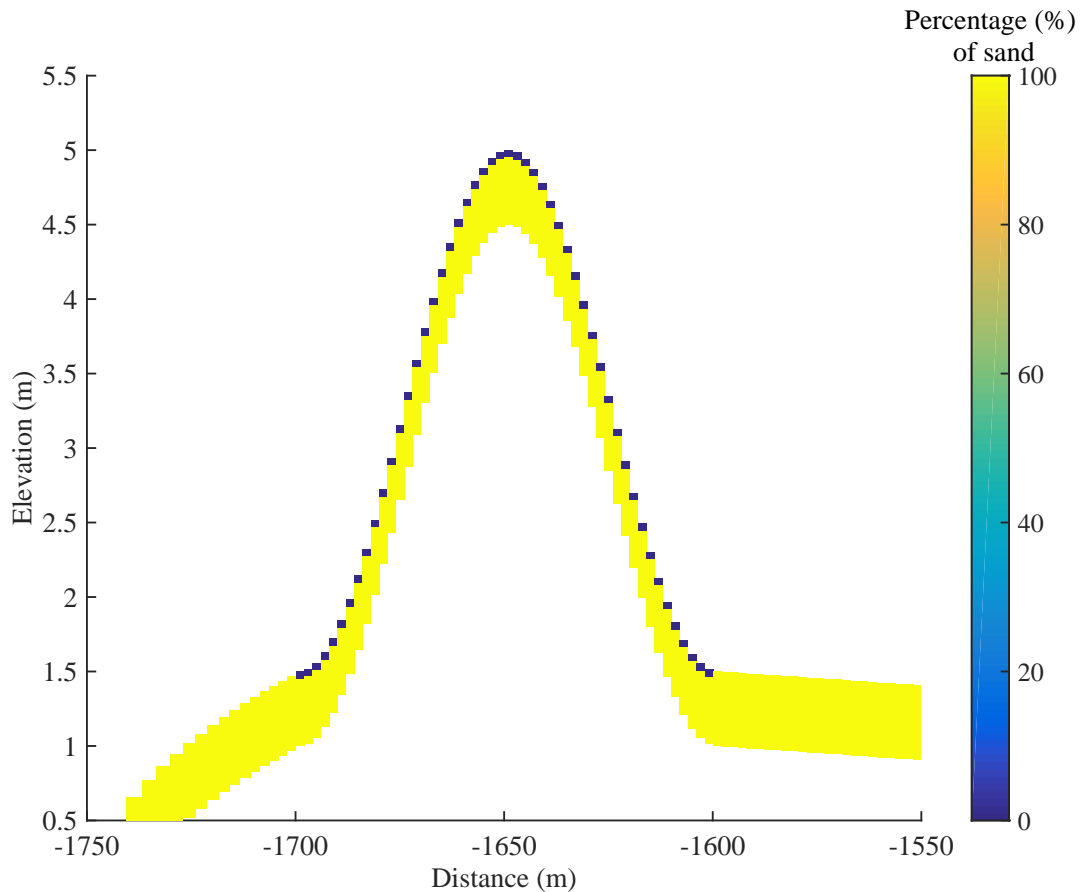


Figure 3.4: Vegetation layer setup. Plot is showing the percentage for grain size class #1.

The top layer contains only grain size #2 (blue), and everywhere else #1 (yellow).

to 0.01, some erosion occurs at the dune, but deposition is limited on the shelf. When sedcal is larger than 0.1, overwash deposition occurs.

Comparing to Fig. 3.6, 75 m berm width (Fig. 3.7) and 100 m (Fig. 3.8) show overall decreasing overwash deposition extent. Within each figure, the sedcal trend is similar to 50 m berm width.

As the berm width further increases to 150 m, the differences between each sedcal value

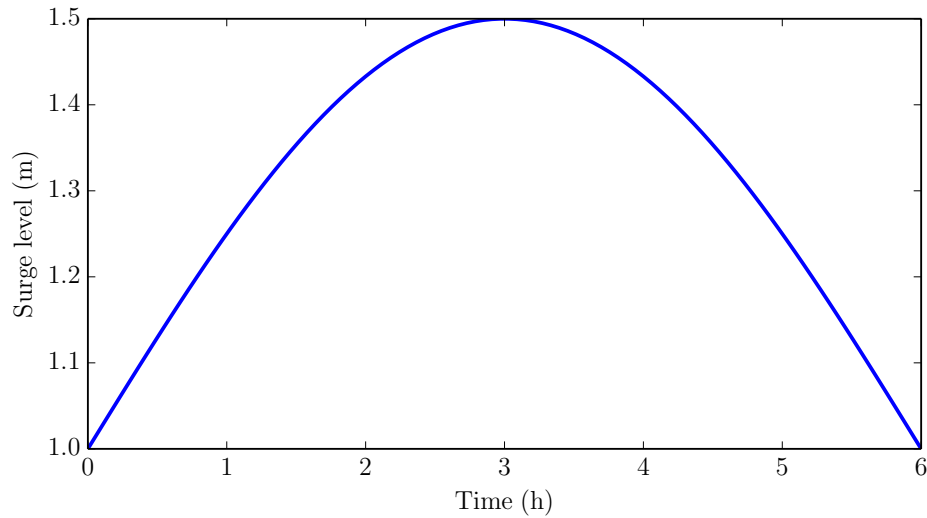


Figure 3.5: Storm surge time series.

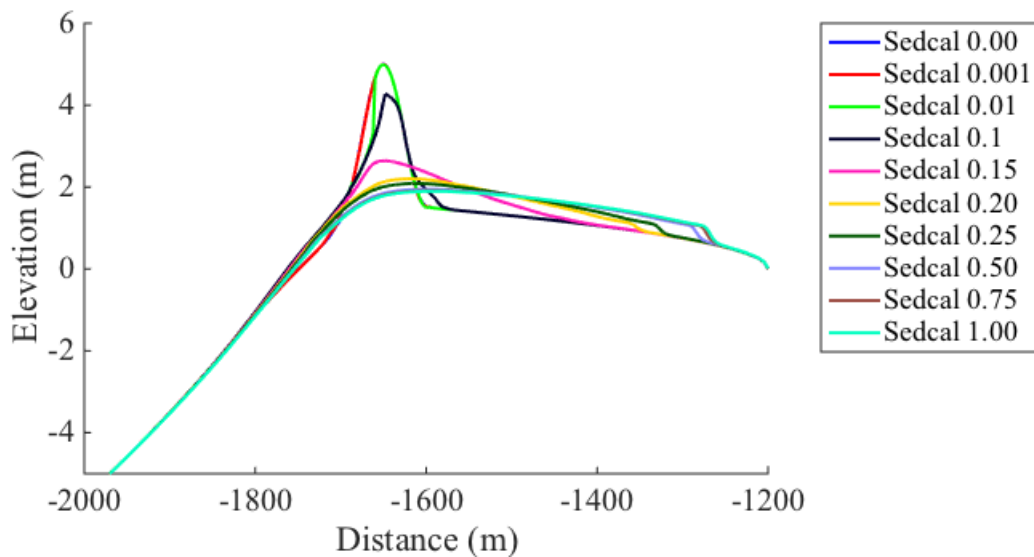


Figure 3.6: Final bed profiles for each sedcal for 50 m berm width.

become less obvious. For example, even when $\text{sedcal} = 1.00$, which is equivalent to no vegetation, there is little erosion of the dune. The control of the berm width over erosion indicates that storm wave energy can be dissipated significantly over the berm, and the wider

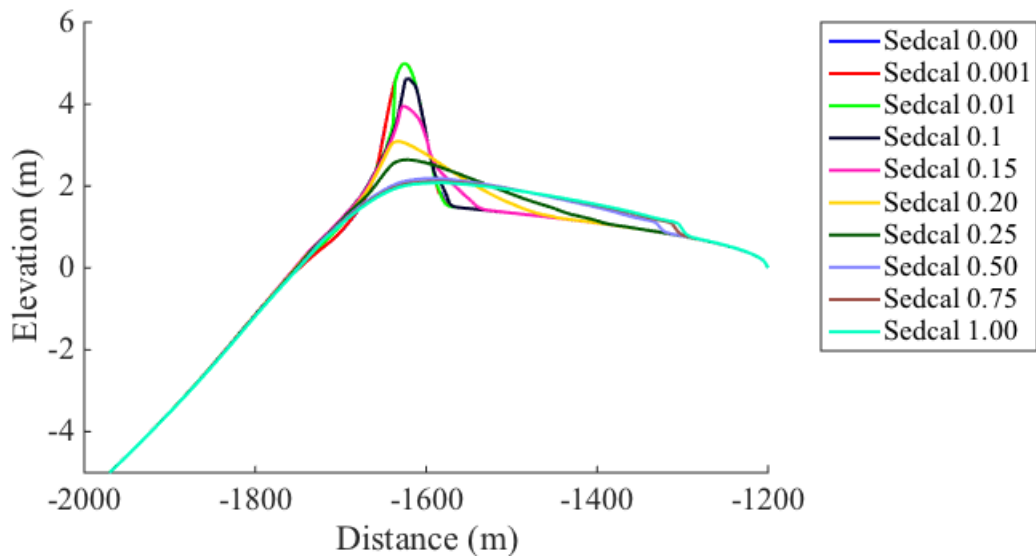


Figure 3.7: Final bed profiles for each sedcal for 75 m berm width.

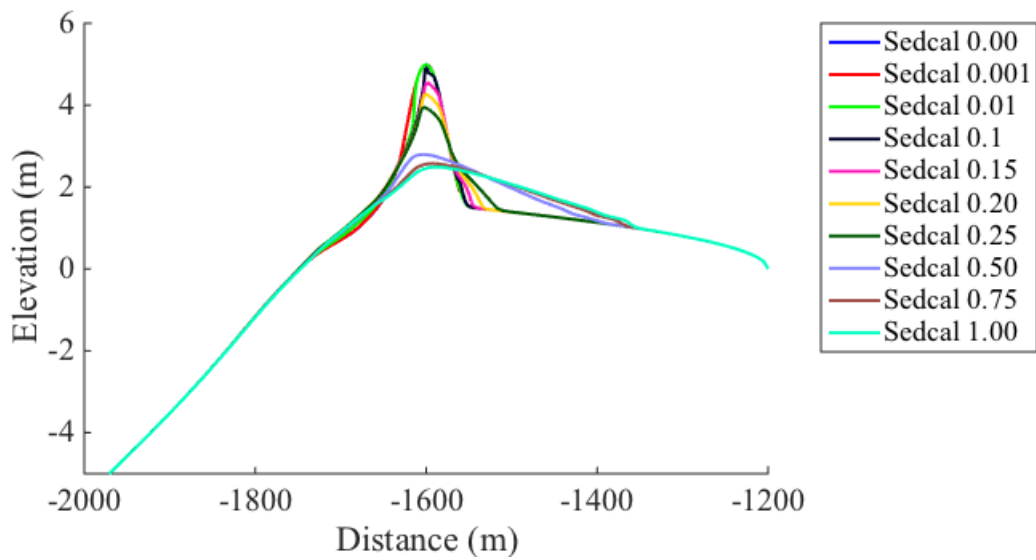


Figure 3.8: Final bed profiles for each sedcal for 100 m berm width.

the berm, the less vulnerable the dune is during a storm of certain strength. The overwash deposition volume, that is, the deposition volume landward of the dune, is plotted against

berm width in Fig. 3.11 for each sedcal value. It can be concluded that for a fixed sedcal, the wider the berm, the more deposition volume, and that for a fixed berm width, larger sedcal results in more deposition. Similar conclusions can be drawn from Fig. 3.12, where the eroded dune height vs. berm width is plotted.

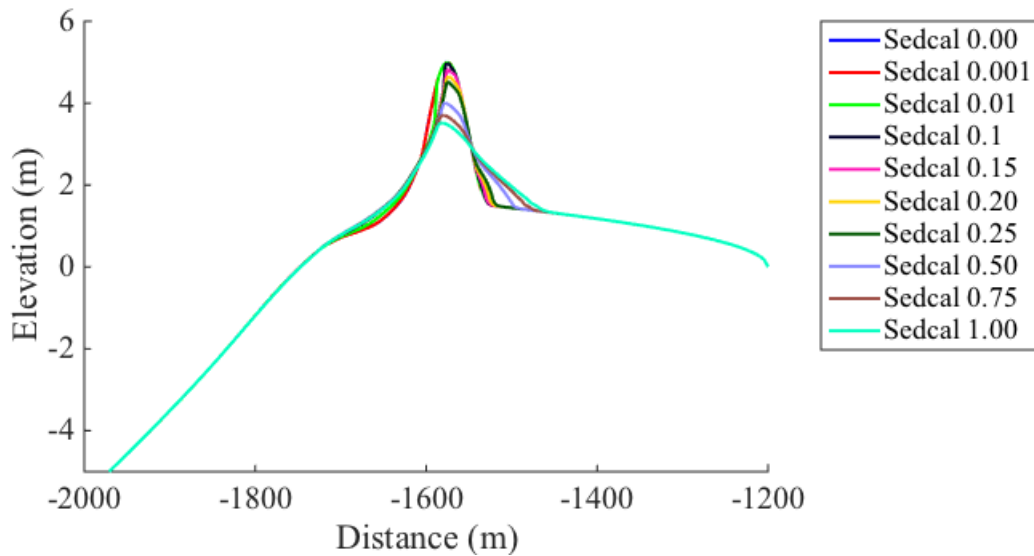


Figure 3.9: Final bed profiles for each sedcal for 125 m berm width.

3.3.5 Discussion

The results from this parameter study involving the berm width and vegetation mobility factor can be employed as a quantitative tool for coastal protection project. For example, using extreme storm conditions for a certain location, the minimum berm width, or distance of the dune from the shoreline, can be determined, that ensures that breaching will not occur.

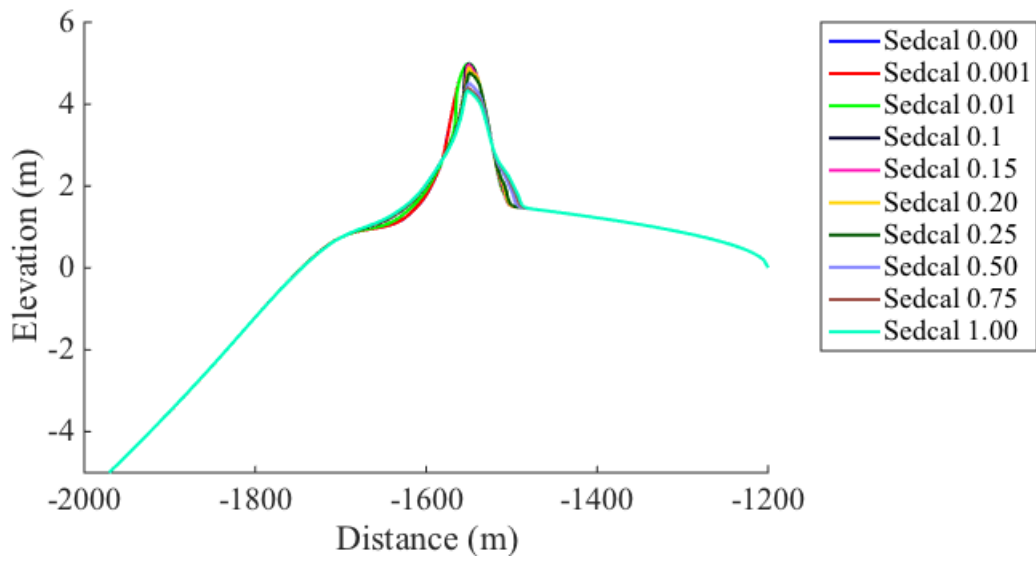


Figure 3.10: Final bed profiles for each sedcal for 150 m berm width.

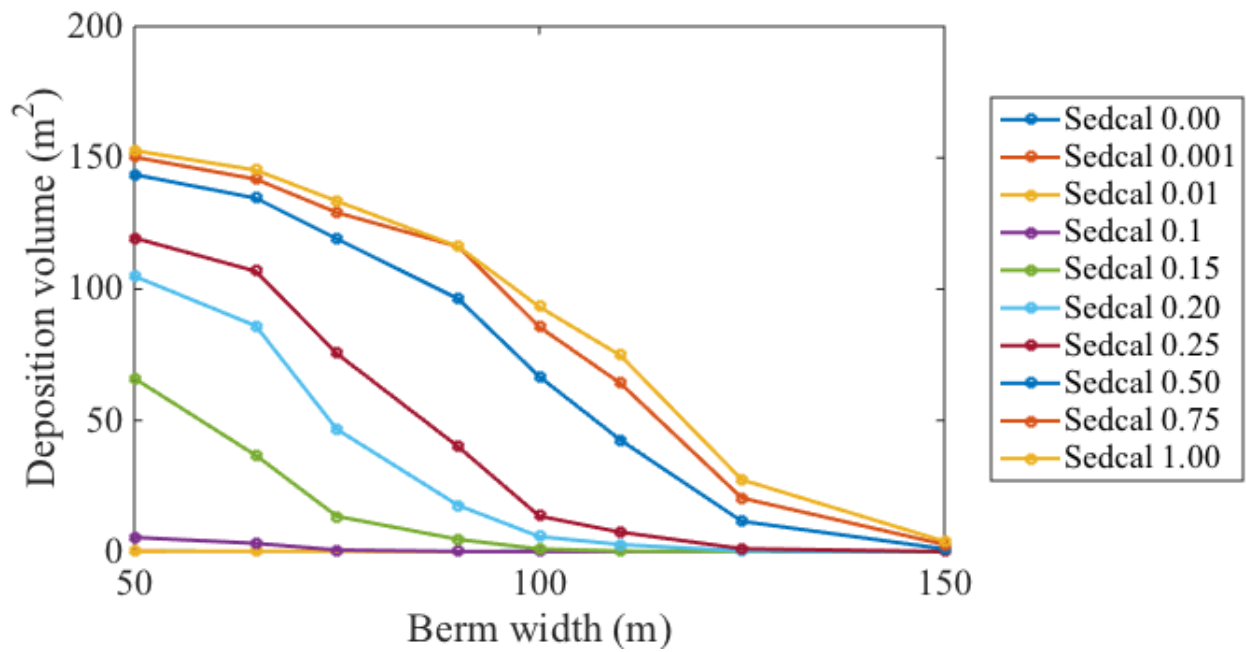


Figure 3.11: Overwash deposition volume vs. berm width.

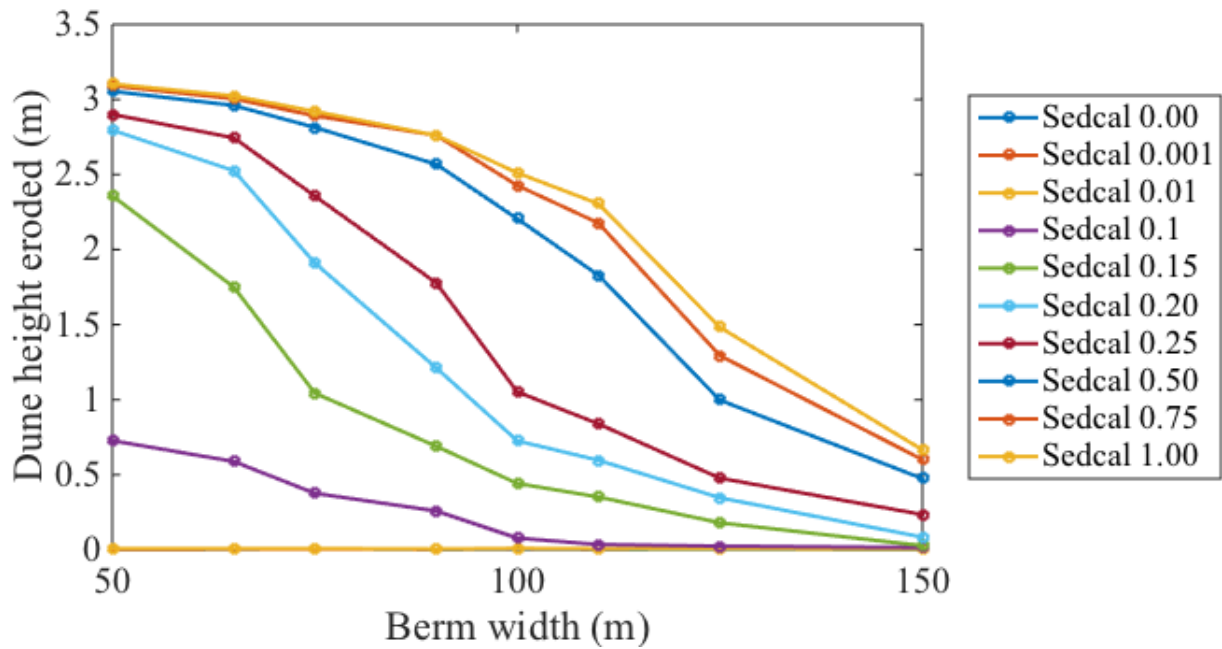


Figure 3.12: Dune height eroded vs. berm width.

The sedcal parameter controls the pickup capability of sediment in XBeach, however, currently this is nothing but a numerical experiment. It is hopeful that through this study, the connection between sedcal and realistic vegetation influence can be found. The current simulations have demonstrated that the berm width and vegetation intensity could significantly influence the barrier island's response to storm impact. To further understand barrier island dynamics, during the next stage, we plan to expand our parameter space to include dune width, dune height, vegetation layer thickness, and sediment properties, as well as extend the computational domain to two dimensional with more realistic storm characteristics.

Chapter 4

The MEso-SCAle Particle Transport model (MESCAPT) for studying sediment dynamics during storms and tsunamis

Abstract

Major tsunamis and storms cause significant casualties and destructions in coastal areas around the world. Deposits of both events play an important role in hazard assessments due

Manuscript (revision #1) submitted to the Journal of Advances in Modeling Earth Systems, Oct 2015, under review.

to the long recurrence intervals. If these event deposits are employed in hazard assessments, firstly storm and tsunami deposits must be separated in the geologic record, and secondly the magnitude of the causative event ought be to decrypted from respective deposit. For the first, several field studies compare both event deposits, but all suffer from the lack of consistent and coherent data. Therefore, an unequivocal set of distinguishing deposit characteristics has not been identified yet. In here, we aim to tackle the problems associated with these two problems with numerical modeling. In this study, we present a MEso-SCAle Particle Transport model (MESCAPT) that combines the advantages of concentration-based Eulerian methods and methods that model individual sediment grains. The meso-scale concept assumes that a small number of sediment grains have the same properties and do not change during transport. Therefore, our model is efficient enough to simulate geophysically interesting domain size and also capable of producing internal sedimentary structures. The sediment transport model is coupled with a hydrodynamic model based on the shallow water equations. Simulation results of a case study show good agreements with field measurements of deposits left behind by the 2004 Indian Ocean Tsunami. Idealized tsunami and storm case studies demonstrate the model's capabilities of reproducing morphological changes, as well as microscopic grain-size trends.

4.1 Introduction

Coastal disasters, such as tsunamis and hurricanes, have caused significant interruption in the lives of coastal communities and resulted into large death tolls. The 2004 Sumatra, 2010 Chile and 2011 Tohoku events are examples for tsunamis, while the 2005 Hurricane Katrina, 2008 Hurricane Ike and 2012 Hurricane Sandy for hurricanes. While on a global scale, these events seem to occur frequently, any given coastline is rarely hit twice within one century with tsunamis or storms of similar magnitude. Especially for tsunamis, the recurrence intervals can be several orders larger than a human lifetime or even historical records. Therefore, the only reliable record of tsunamis, as well as storms, are the deposits that both events leave behind. Reliable hazard assessments for storms and tsunamis have to merge from respective event statistics that are based on respective deposits. However, in areas where storms and tsunamis are competing disasters, it is pivotal to distinguish between both events in the geologic record.

Because storm and tsunami deposits are recordings of the respective causative process (Huntington et al., 2007), information of the causative process is encrypted in the structural content of the deposit. The decryption of the information about the causative event in the deposits is very important for hazard assessment; however, equally important is the ability to distinguish between storm and tsunami deposits in areas where both events occur as competing disasters as mentioned earlier. There have been a number of studies tackling the issue of distinguishing between storm and tsunami deposits. The general parameters that have been

looked at include thickness of the deposits, thickness trends, grain-size trends, and sedimentary structures or the lack thereof (Nanayama et al., 2000; Goff et al., 2004; Tuttle et al., 2004; Kortekaas and Dawson, 2007; Morton et al., 2007). Notably, Morton et al. (2007) summarized the hydrodynamics and deposit characteristics of both tsunamis and storms and distilled the most diagnostic features that allow effective differentiation. However, it is still being discussed in the literature if it is impossible to produce unequivocal evidence that separates a random tsunami from random storm deposit that is based solely on the deposits.

Based on the extensive list of hydrodynamic differences between storm and tsunamis, we think that careful numerical modeling can help to overcome this shortcoming. In here, we present a meso-scale sediment transport model for storm and tsunami hydrodynamics that aims at reproducing the internal structure of the tsunami and storm deposits. In our model we define meso-scale particles to represent a small number of actual sediment grains. The transport of the meso-scale particles is computed with the help of Newton's Second Law of Motion. Our method is in a sense similar to sediment transport models that employ sediment particles directly. However these particle-based models can only consider a domain that is usually not larger than a few square centimeters (e.g., Calantoni et al., 2004). The meso-scale particles help us to extend the domain to meaningful sizes and also allow us to simulate the sediment dynamics in high accuracy to resolve the internal structure of the generated storm and tsunami deposits.

4.2 Theoretical Background

4.2.1 The Meso-scale Concept

A continuous sediment concentration distributed in the water column that experiences diffusion and advection is the most common assumption to approach sediment transport, because it could efficiently model spatial scales that have geophysical relevance. An alternative approach considers each sediment particle individually. As mentioned earlier, the second approach restricts the domain sizes to mere square centimeters at the most. Fig. 4.1a depicts the concept of the concentration-based approach. The black solid circles represent sediment particles. An Eulerian grid is employed to define the concentration in each cell, which corresponds to the number of sediment particles per unit volume. In the particle-based approach, an equation of motion for each particle is solved as well as the interaction between particles, for example, collision is parametrized, resulting into a computationally challenging problem because of the very large number of particles. However, the location of each particle at each time step is very well determined, and it makes tracking the sources and sinks of sediments possible (Cooper et al., 2012). In addition, an advantage of particle models is that conservation of mass is automatically satisfied.

In the Eulerian method, the physical scale at which changes in the concentration distribution can be simulated depends on the numerical technique employed to solve the governing equations, but averaging scale is at least two Δx , where Δx represents the size of the Eulerian cells. For tsunami and storm sediment transport, whose hydrodynamics is often modeled

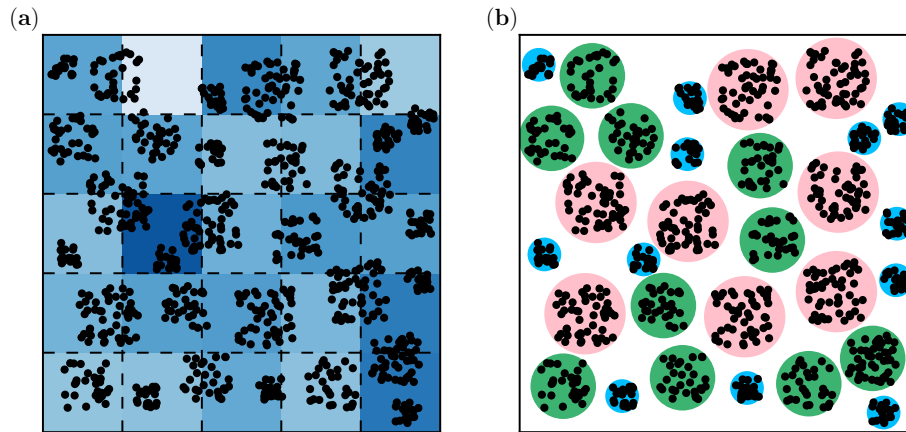


Figure 4.1: Illustration of comparison between conventional grid-based methods for sediment transport (a) and meso-scale particles (b). Black dots denote sediment grains, and colored circles denote meso-scale particles of different sizes. Colored grid in (a) shows the concentration of the sediments, with darker blue indicating higher concentration.

with the depth-averaged Shallow Water Equations, the Eulerian representation is reduced to a two-dimensional horizontal problem. This simplification results into a depth-averaged concentration with a subsequent impact on the vertical resolution of the generated deposits. This fact together with the spatially horizontal averaging ($2 \Delta x$) makes it impossible for these models to reproduce the internal structure of storm and tsunami deposits with confidence.

Recently, hybrid Eulerian-Lagrangian models (ELM) have become popular due to the need for more detailed information on sediment transport and spatial distributions and model efficiency. The marker-in-cell (MiC) method has been adopted by many researchers to study sediment transport in a variety of settings, such as atmospheric pollutant transport (e.g., Lange, 1973; Lange and Knox, 1974), and dredged material disposal (e.g., Johnson, 1974).

The MiC method originated from the particle-in-cell (PiC) method by Evans et al. (1957) to model fluid dynamics. In PiC methods, fluid field solved at grid scale is used for the motion of fluid particles, and the new fluid particle positions are then mapped onto the cells, completing a two-way interaction. Similarly, cell-based fluid velocities are used to drive solid particles in MiC, however, usually there is only one-way coupling, i.e., particle motion does not feedback to the flow. For example, Spaulding and Pavish (1984) developed a 3D Lagrangian particle transport model for pollutant transport in estuarine and coastal settings. In their model, advective velocities calculated from the Eulerian model and the diffusive velocities calculated from concentration are added together to move the Lagrangian particles. Cooper et al. (2012) developed a sediment transport model for soil erosion on hillslopes during rainfalls using the marker-in-cell method. The hydrodynamic component of the cell-based model, MAHLERAN, was used in conjunction with a particle-based MiC model. Several rainfall and hillslope associated processes, for example raindrop erosion, rain splash transport, interrill sediment erosion and transport, and bed load, have been included in the model. The model shows good agreement compared to the spatial and temporal distribution of soil in a single rainfall experiment.

Another type of method handles sediment differently. Instead of tracking particles everywhere, a hybrid approach is employed that only uses particles for sediment transport and use cells to represent sediment at rest. Bozzi and Passoni (2012) presented a hybrid model for bottom evolution due to particle erosion and deposition. The 2D incompressible Navier-Stokes equations were solved by the finite volume model FLUENT for the hydrodynamics. A

Lagrangian particle method was used to model the deposition, resuspension, and transport of sediment of a single grain size. The bed elevation changes as particles deposit or erode, and the particle volume is added to or subtracted from the bottom cells, respectively. Notably in their model computational particles with fictional mass are used instead of individual sediment grains by assuming that all the real grains within a computational particle follow the same path. Our meso-scale particle concept is similar to their computational particle.

We argue that a meso-scale approach that combines the advantages of Eulerian and particle methods, where the advantage of the Eulerian method is the ability to consider geophysically relevant domain sizes and the advantage of the particle method is its accuracy to determine the location of the particles. Fig. 4.1b depicts the approach. The circles represent meso-scale particles whose size is determined by the number of sediment particles that make them up. The movement of each meso-scale particle is computed with an equation of motion like in the particle model. Because a group of sediment particles make up a meso-scale particle, we can simulate geophysically interesting domain sizes. The preserved three dimensional character of the equations governing the movement of the meso-scale particles results into the ability of this approach to reconstruct the internal structures of storm and tsunami deposits, also known as their stratigraphy, with the confidence of the three dimensional and physically appropriate model.

4.2.2 Governing Equations for Meso-scale Particle Transport

Equation of Motion

Meso-scale particles in our model refer to a small number of sediment grains. We make the following assumptions regarding the erosion/generation, transport and deposition of the meso-scale particles. First, at each time step, once the amount of erosion is calculated with Eq. 4.4 for grain size class θ , a meso-scale particle Θ is generated. This meso-scale particle Θ has a volume that is the sum of the sediments picked up. Therefore a meso-scale particle is always composed of sediment grains of the same size. During transport, we assume that the volume of Θ does not change, i.e., Θ does not merge with other meso-scale particles, nor does it break up into smaller ones. The whole group of sediment grains in Θ follows the same motion as if there were only a single grain of size θ . In another word, the volume of Θ does not affect its motion, and there is no interactions between the grains inside Θ .

Meso-scale particles are designed to increase the efficiency of computation. However, generating meso-scale particles at each time step is still not feasible since a typical grid with just hundreds of cells could easily be populated with tens of millions of particles which cannot be handled efficiently. Therefore we introduce a morphological acceleration parameter Σ that can help with this situation. For every Σ seconds, we calculate the amount of erosion for a meso-scale particle, which is then multiplied by $\Sigma/\Delta t$, assuming this erosion rate is the average. Preliminary parameter study shows that results are stable using hundreds of time steps for Σ . Traditional morphological acceleration parameter in sediment transport models,

for example XBeach (Roelvink et al., 2009), speeds up calculation by simply multiplying sediment transport flux, which can be used to accelerate the simulations of cyclic water motion such as tides over a long period of time. Therefore the traditional method is not suitable for our study where hydrodynamic conditions change rapidly and are not cyclic.

Vertically, particle movement is governed by the following equation of motion (Newton's Second Law of Motion):

$$\begin{aligned} V_s \rho_s \frac{d\vec{v}_s}{dt} &= \vec{F}_{gravity} + \vec{F}_{buoyancy} + \vec{F}_{drag} \\ &= V_s \rho_s \vec{g} - V_s \rho_f \vec{g} - \text{sign}(\vec{v}_s) \frac{1}{2} C_{drag} \rho_f \pi r^2 |\vec{v}_s|^2 \end{aligned} \quad (4.1)$$

where $F_{gravity}$, $F_{buoyancy}$ and F_{drag} are different forces, V is sediment grain volume, ρ is density, v is vertical velocity, g is gravitational acceleration, C_{drag} is the drag coefficient, r is sediment grain radius. Subscript s denotes the sediment, and subscript f the fluid. The drag coefficient C_{drag} is calculated using (Morrison, 2013):

$$C_D = \frac{24}{Re} + \frac{2.6 \left(\frac{Re}{5.0}\right)}{1 + \left(\frac{Re}{5.0}\right)^{1.52}} + \frac{0.411 \left(\frac{Re}{263000}\right)^{-7.94}}{1 + \left(\frac{Re}{263000}\right)^{-8.00}} + \left(\frac{Re^{0.80}}{461000}\right) \quad (4.2)$$

Eq. 4.2 is data correlation based on uniform flow around sphere experiments by Schlichting et al. (2000). Eq. 4.2 covers the full range of Reynolds number for spherical particles. Note that there is sediment contribution to water density ρ_f in each cell, as a result, hindered settling will occur where sediment concentration is high. The varying water density only applies to the sediment transport and does not feedback to the hydrodynamics. Hindered settling can also be caused by particle interactions and water flowing in the opposite direction as the particles settle (Middleton et al., 2003), however, these two processes are not included

in our model. In the horizontal direction, particle velocity u is calculated from the velocity profile equations (Eq. 4.20) that will be introduced later.

The velocity vector $\mathbf{V} = (u, v)$ is used to update the particle position with $\mathbf{X}^{n+1} = \mathbf{X}^n + \mathbf{V}\Delta t$, where the superscript indicates variables at different time, and Δt is the time step. A particle leaves the domain when it reaches the lateral boundaries. In the vertical direction, the meso-scale particles are bounded by the water surface. Particle deposition and erosion will be introduced in the following.

Deposition and Erosion

The main difference between our model and MiC (e.g., Cooper et al., 2012), is that we use cells to represent deposited sediment particles, and only convert to particles when erosion occurs, whereas, particles/markers do not change even when deposited in MiC models. The advantage of using cells for the deposited sediment is that more particles are allowed to be simulated for the same amount of computational resources and particle collision is avoided.

For deposition, we define vertical columns that have the same width $\Delta\xi$ (Fig. 4.2). Inside each deposition column, deposit is modeled as a vertical stack of thin layers that have the same thickness. Deposition occurs when sediment particles reach bed surface. If a meso-scale particle is deposited, we assume that its actual sediment grains are evenly distributed across the entire width of $\Delta\xi$. The thickness that this deposited meso-scale particle occupies, taking into account the porosity, is added to that of the same grain-size fraction in the top

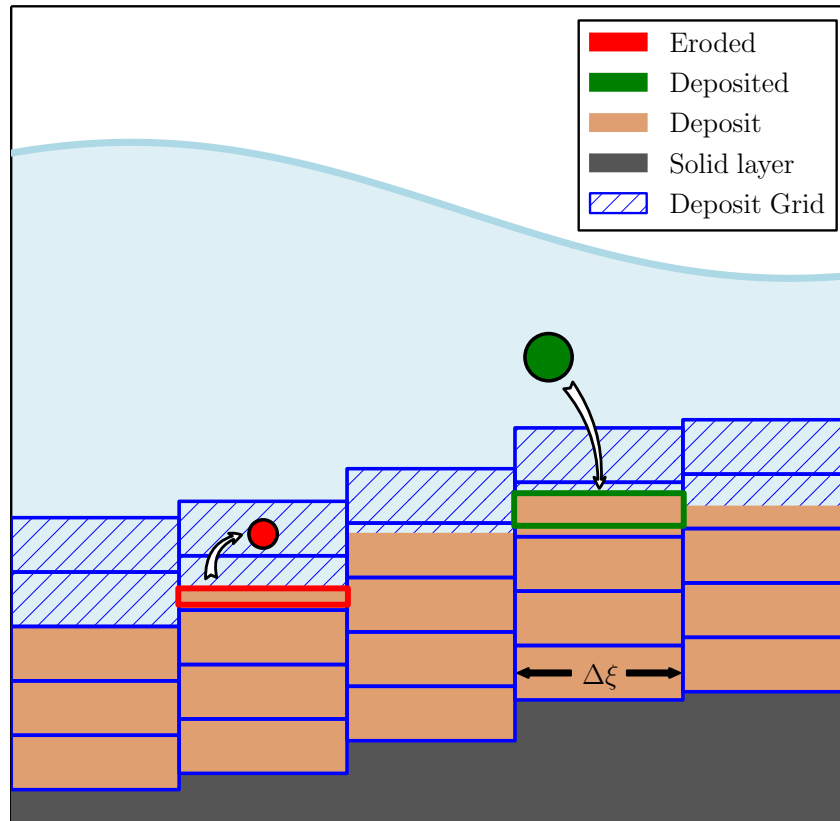


Figure 4.2: Deposition grid with illustrations of erosion and deposition of meso-scale particles. Dark grey color denotes solid layer. Blue rectangles form the deposition grid. Beige color denotes deposits. Red solid circle is a newly generated particle. Green solid circle is a particle that will be deposited.

layer. When the combined thickness of all grain-size fractions exceeds the predefined layer thickness, a new layer is created above, accepting deposition.

The angle of repose constrains the maximum slope of the deposits. If a slope exceeds the angle of repose, bed sliding is triggered. The angle of this threshold was experimentally determined to be 37° (equivalent to a 3 : 4 slope) by Spinewine et al. (2002) for uniform

sand. In their experiment the flow velocity was negligible. Therefore this angle corresponds to a pure slumping slope. Considering both the tremendous wave forcing of tsunamis and storms and the variability in coastal sediments, we chose 3 : 10 as the threshold slope (e.g., Roelvink et al., 2009). At each time step and between each cell interface, bed sliding flux Δz_b is calculated with the following equation:

$$\Delta z_b = \min \left(\left(\left| \frac{\partial z_b}{\partial x} \right| - S_{wet} \right) \frac{\Delta x}{2}, \dot{z}_{max} \Delta t \right) \quad (4.3)$$

where S_{wet} is the submerged critical slope and \dot{z}_{max} is the maximum bed sliding flux per time step.

In conventional concentration-based sediment transport methods (e.g., Wu, 2004), sediment exchange between water and bed is achieved by comparing depth-averaged concentration and equilibrium concentration for suspended-load transport, or transport rate and transport capacity for bed-load transport. However, for particle-based sediment transport system, it is unnecessary to differentiate suspended from bed load, because once a particle is dislodged into the water, its fate is determined solely by the flow. This unifies the numerical modeling of erosion, as well as sediment transport.

The amount of sediment entrained is calculated with pick-up functions. We use the one proposed by van Rijn (1984):

$$\omega_i = 0.00033 (\Delta g d_{50})^{0.5} \left[d_{50} \left(\frac{\Delta g}{\nu^2} \right)^{\frac{1}{3}} \right]^{0.3} \left[\frac{(u_*)^2 - (u_{*,i}^{cr})^2}{(u_{*,i}^{cr})^2} \right]^{1.5} \quad (4.4)$$

in which ω_i is the volumetric pick-up rate for the i th grain-size fraction, $\Delta = (\rho_s - \rho_f) / \rho_f$, d_{50} is the median grain size, $\nu = 10^{-6} m^2/s$ is the kinematic viscosity (used throughout the text), u_* is shear velocity, and $u_{*,i}^{cr}$ is the Shields critical shear velocity for the i th grain size.

To calculate the shear velocity u_* we employ the law of the wall:

$$u_* = u\kappa \frac{h - z_0}{z_0 - h + h \log(h/z_0)} \quad (4.5)$$

where u is the mean flow velocity. κ is the van Karman's constant (≈ 0.41). The parameter z_0 is the reference height above the wall, for which we assume Nikuradse's roughness length, $z_0 = d_{50}/30$. Note that d_{50} is the median diameter for the surface layer.

After the amount is obtained, the starting position of the meso-scale particle needs to be determined. For the vertical position, we chose a distance that scales with the bed-load layer height. Smith and McLean (1977) proposed a bed layer height:

$$h_b = 0.056 (u_*^2 - u_{*,i}^{cr}) \frac{\rho_f}{(\rho_s - \rho_f)g} \quad (4.6)$$

Horizontally, the newly generated meso-scale particle is positioned at the center of a deposition column. The initial velocity of this particle is set to zero.

Turbulent Suspension

A statistical approach is employed in the current hydrodynamic model to represent the influence of turbulence on particle suspension (Matida et al., 2000). Eddies with a characteristic

size, velocity and lifetime that scale with the primary flow are generated to interact with particles (e.g., Graham and James, 1996). This approach utilizes existing 2D channel flow DNS data to simulate fluctuating velocities. Specifically, the Root Mean Square (RMS) values of the velocity fluctuations in each direction obtained from curve-fitted DNS data are used in conjunction with random number generation to form eddies that interact with particles. It is worth noting that turbulent suspension is solely for the purpose of particle motion, and thus doesn't affect the primary flow.

At each time step, and for each particle, the following values are calculated:

$$\begin{aligned}
 u'_{rms} &= u_* \frac{0.40 z^+}{1 + 0.0239 (z^+)^{1.496}} \\
 v'_{rms} &= u_* \frac{0.0116 (z^+)^2}{1 + 0.203 z^+ + 0.00140 (z^+)^{2.421}} \\
 \varepsilon^+ &= \frac{1}{4.529 + 0.0116 (z^+)^{1.75} + 0.768 (z^+)^{0.5}}
 \end{aligned} \tag{4.7}$$

where $z^+ = z u_* / \nu$ is the dimensionless distance from wall, u'_{rms} and v'_{rms} are the RMS values of the horizontal and vertical velocity fluctuations, respectively, and ε is the dissipation in k-epsilon turbulence model. The + superscript denotes wall non-dimensionalized variables.

For each meso-scale particle, an eddy is generated initially centered around the particle with eddy lifetime τ_e , fluctuating velocities u_e and v_e , and eddy radius L_e , defined as:

$$\begin{aligned}\tau_e &= C_1 \frac{(v'_{rms})^2}{\varepsilon} \\ (u_e, v_e) &= (N_u u'_{rms}, N_v v'_{rms}) \\ L_e &= \tau_e u_e\end{aligned}\tag{4.8}$$

where N_u and N_v are random numbers generated from standard normal distribution, which are kept constant during the lifetime of an eddy. The eddy lifetime τ_e was chosen as $2\tau_L$ to ensure dispersion consistency, following the work of Graham and James (1996). The Lagrangian integral timescale τ_L is estimated by Hinze (1975) as $\tau_L \sim C_2 k / \varepsilon$ in homogeneous isotropic stationary turbulence, where the turbulence kinetic energy k is proportional to v'^2_{rms} , assuming wall-normal velocity fluctuations v'_{rms} is appropriate for the time scale. Finally, C_1 is optimized to be 1.0 to fit to the experiment data from Liu and Agarwal (1974).

Each eddy updates its position with its velocities u_e and v_e . The eddy velocity also updates according to the new distance from the wall. At the same time, the particle that was initially at the center of the eddy when newly generated, updates its position based on the mean flow and the fluctuating eddy velocities. Once this particle falls outside the eddy, a new eddy is generated. The above procedures repeat until the particle deposits.

4.2.3 Hydrodynamic Model

Shallow Water Equations

For simplicity and efficiency, the one-dimensional non-linear shallow water equations are used to model long wave propagation:

$$\begin{aligned} \frac{\partial h}{\partial t} + \frac{\partial (hu)}{\partial x} &= 0 \\ \frac{\partial (hu)}{\partial t} + \frac{\partial}{\partial x} \left(hu^2 + \frac{1}{2}gh^2 \right) &= -gh \frac{\partial z}{\partial x} - ghf \\ f &= n^2 \frac{u|u|}{h^{4/3}} \end{aligned} \quad (4.9)$$

where h and u are the water depth and horizontal velocity, respectively, z is the bed elevation, n is the Manning coefficient and f the friction term.

Eq. 4.9 can be rearranged into a conservation form,

$$\frac{\partial \mathbf{q}}{\partial t} + \frac{\partial}{\partial x} \mathbf{F}(\mathbf{q}) = \mathbf{R} + \mathbf{S} \quad (4.10)$$

where

$$\mathbf{q} = \begin{bmatrix} h \\ uh \end{bmatrix}, \quad \mathbf{F} = \begin{bmatrix} uh \\ hu^2 + \frac{1}{2}gh^2 \end{bmatrix}, \quad \mathbf{R} = \begin{bmatrix} 0 \\ -gh \frac{\partial z}{\partial x} \end{bmatrix}, \quad \mathbf{S} = \begin{bmatrix} 0 \\ -ghf \end{bmatrix} \quad (4.11)$$

This set of equations is solved with the popular Roe-type Riemann solver (Roe, 1997) using Finite Volume Method. The space domain is discretized so that $x_i = i\Delta x$ is at the grid points and $x_{i\pm 1/2} = (i \pm \frac{1}{2}) \Delta x$ at the interfaces, where Δx is constant. The time domain is discretized by letting $t^{n+1} = t^n + \Delta t^n$. The cell average of the conserved variable \mathbf{q} is denoted as $\mathbf{Q}_i(t) = \int_{x_{i-1/2}}^{x_{i+1/2}} \mathbf{q}(x, t) dx$.

Considering the approximate solution \mathbf{Q}_i^n at time t^n , Eq. 4.10 can be rewritten as,

$$\mathbf{Q}_i^{n+1} = \mathbf{Q}_i^n - \frac{\Delta t^n}{\Delta x} [\mathbf{F}_{i+1/2}^n - \mathbf{F}_{i-1/2}^n] + \frac{\Delta t^n}{\Delta x} \left[\left(\mathbf{R}_{i+1/2}^- \right)^n + \left(\mathbf{R}_{i-1/2}^+ \right)^n \right] + \Delta t^n \mathbf{S}_i^n \quad (4.12)$$

Using Roe's flux difference splitting scheme, the interface flux vector is defined as,

$$\mathbf{F}_{i-1/2}^n = \frac{1}{2} (\mathbf{F}_{i-1}^n + \mathbf{F}_i^n) - \frac{1}{2} \sum_{p=1}^2 \left[|\lambda_p| \alpha_p \mathbf{r}_p \left(1 - \Phi(\theta_p) \left(1 - \frac{\Delta t^n}{\Delta x} |\lambda_p| \right) \right) \right]_{i-1/2}^n \quad (4.13)$$

where

$$\begin{aligned} (\lambda_1)_{i-1/2}^n &= u_{i-1/2} - c_{i-1/2}, \quad (\lambda_2)_{i-1/2}^n = u_{i-1/2} + c_{i-1/2} \\ \mathbf{r}_1 &= \begin{bmatrix} 1 \\ (\lambda_1)_{i-1/2}^n \end{bmatrix}, \quad \mathbf{r}_2 = \begin{bmatrix} 1 \\ (\lambda_2)_{i-1/2}^n \end{bmatrix} \end{aligned} \quad (4.14)$$

are the eigenvalues and eigenvectors of the Jacobian matrix $\mathbf{A}_{i-1/2}^n$ between \mathbf{Q}_{i-1}^n and \mathbf{Q}_i^n ,

which is defined as,

$$\mathbf{A}_{i-1/2}^n = \begin{bmatrix} 0 & 1 \\ \left(c_{i-1/2}^n \right)^2 - \left(u_{i-1/2}^n \right)^2 & 2u_{i-1/2}^n \end{bmatrix} \quad (4.15)$$

where

$$c_{i-1/2}^n = \sqrt{g \frac{h_{i-1}^n + h_i^n}{2}}, \quad u_{i-1/2}^n = \frac{u_{i-1}^n \sqrt{h_{i-1}^n} + u_i^n \sqrt{h_i^n}}{\sqrt{h_{i-1}^n} + \sqrt{h_i^n}} \quad (4.16)$$

The Lax-Wendroff numerical flux, has been incorporated in Eq. 4.13, to extend the first-order upwind scheme to high-order (Delis et al., 2008). The resulting high-order scheme ensures the total variation diminishing (TVD) property. $\Phi(\cdot)$ denotes the flux-limiting function. While a number of different functions can be used, the Minmod flux-limiter is employed. θ_p

is defined as,

$$\theta_p = \frac{(\alpha_p)_{s-1/2}}{(\alpha_p)_{i-1/2}}, \quad s = \begin{cases} i-1 & \text{if } \lambda_p > 0 \\ i+1 & \text{if } \lambda_p < 0 \end{cases} \quad (4.17)$$

The corresponding high order source term can be expressed as,

$$\mathbf{R}_{i-1/2}^{\pm} = \frac{1}{2} \sum_{p=1}^2 \left[\beta_p \mathbf{r}_p \left(1 \pm \text{sign}(\theta_p) \left(1 - \Phi(\theta_p) \left(1 - \frac{\Delta t^n}{\Delta x} |\lambda_p| \right) \right) \right) \right]_{i-1/2} \quad (4.18)$$

where

$$(\beta_{1,2})_{i-1/2} = \pm \frac{c_{i-1/2} (z_i - z_{i-1})}{2} \quad (4.19)$$

Wetting and drying is also implemented to handle inundation. (Castro et al., 2005)

Velocity Profile

To be able to couple the SWE with the meso-scale particle sediment transport model, both the horizontal velocity u and vertical velocity v need to be obtained everywhere inside the water body. Sitanggang and Lynett (2010) developed a hybrid model where 1D Boussinesq model solutions are converted to velocity profiles and passed on to a neighbor domain that is solved with a 2D RANS model. Here we use the same idea to obtain the horizontal and vertical velocity components from SWE solutions. The former is achieved by vertically integrating the irrotationality condition, while the latter from the continuity equation (Wei et al., 1995):

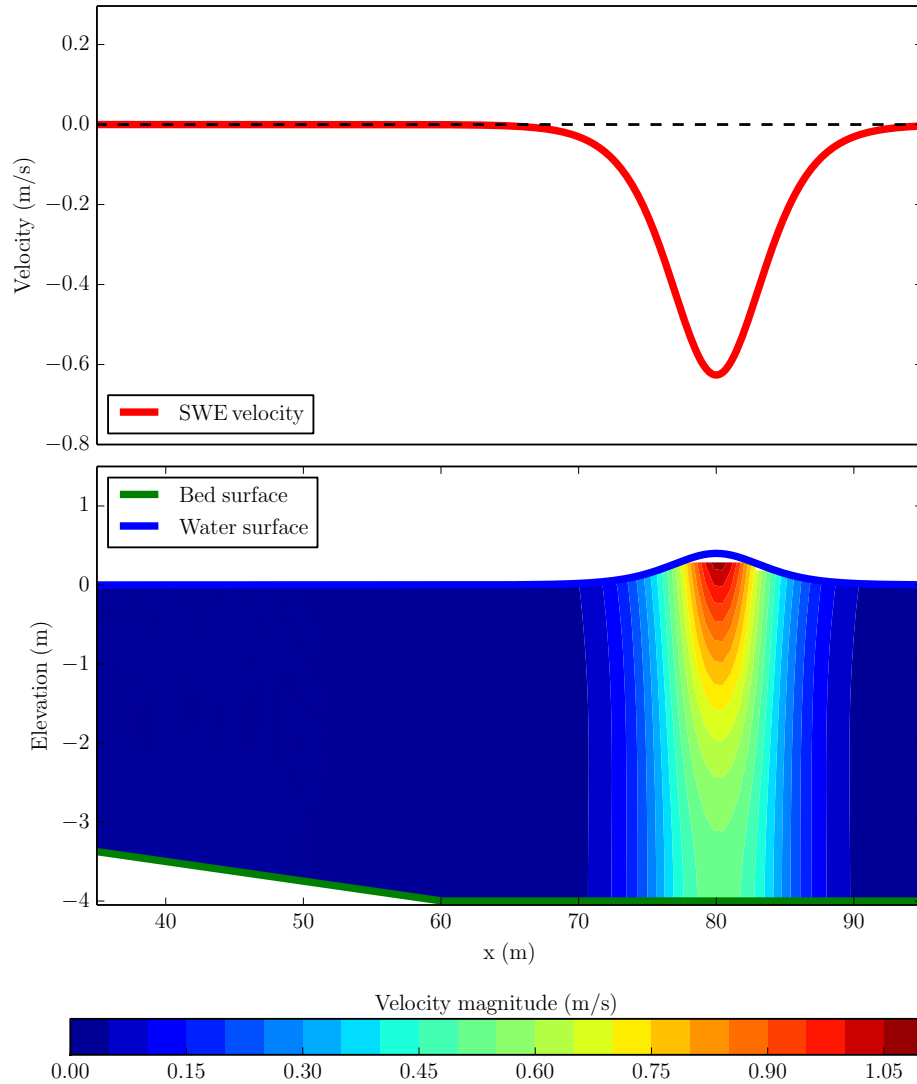


Figure 4.3: Inverted velocity profile for an initial solitary wave of amplitude 0.4m. Top pane shows the shallow water velocity for this wave. Bottom pane is a contour plot of the velocity magnitude.

$$\begin{aligned}
u(x, z) &= u_\alpha + \frac{1}{2} (z^2 - z_\alpha^2) \frac{d^2 u_\alpha}{dx^2} + (z - z_\alpha) \frac{d^2 (hu_\alpha)}{dx^2} \\
v(x, z) &= -z \frac{du_\alpha}{dx} - \frac{d(hu_\alpha)}{dx}
\end{aligned}
\tag{4.20}$$

where u and v are the horizontal and vertical particle velocity, respectively, x and z are the horizontal and vertical position, respectively. Subscript α denotes variables at the reference level used in Boussinesq models (e.g., Nwogu, 1993). The reference level z_α is $-0.531h$, and u_α is calculated using law of the wall, where h is the distance from the bed to the still water level.

Fig. 4.3 shows the original shallow water model velocity and the inverted velocity profile. In this example, a 0.4 meter solitary wave is traveling to the left in a 4 meter deep region. Intuitively, the wave crest corresponds to higher velocities, comparing to farther away from the crest both horizontally and vertically. The maximum SWE average horizontal velocity is about 0.63 m/s, while the maximum horizontal component of the velocity profile is 1.08 m/s, which is close to the surface. After the velocity components at any given position are calculated, they are superimposed on particles to represent the influence of the wave.

Hydrodynamic Model Validation

Numerical results from the hydrodynamic model are validated against several benchmark problems, including solitary wave run-up on a plane beach (Synolakis, 1987), tsunami run-up onto a plane beach (Delis et al., 2008), and a 2D landslide triggered tsunami run-up (Liu et al., 2003). Our simulation results show satisfactory agreements with both analytical

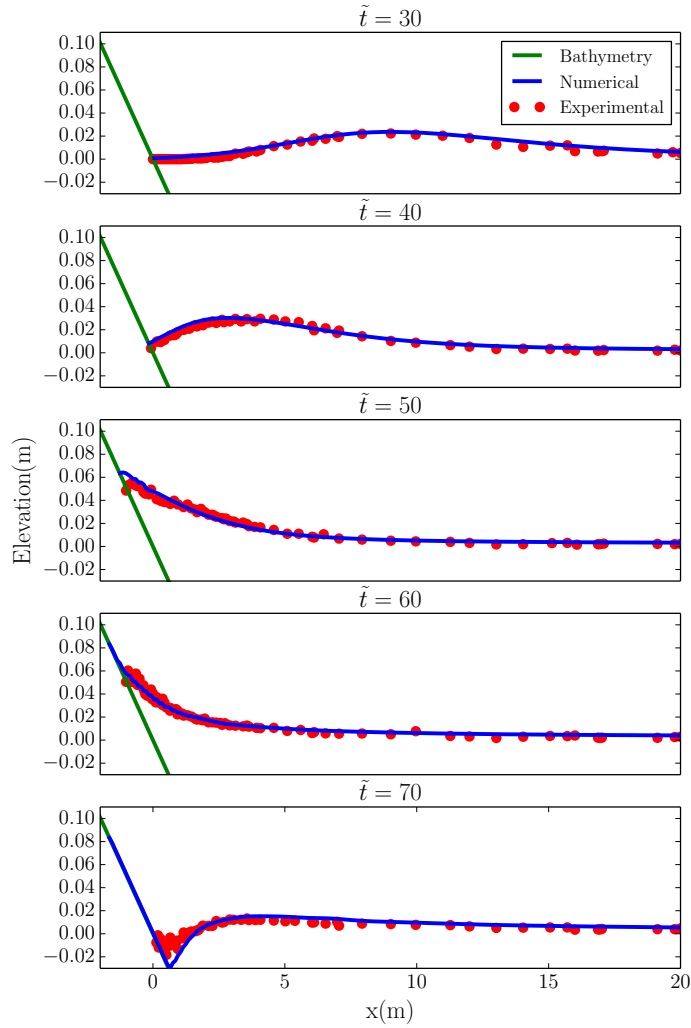


Figure 4.4: Comparison between numerical simulation results and experimental data of an $h/D = 0.0185$ non-breaking solitary wave running up on a single slope. Results show very good correlation.

solutions and experimental data from the above benchmark sources.

Fig. 4.4 demonstrates very good agreements between Synolakis (1987) experimental data and our simulation results for the $h/D = 0.0185$ case at normalized times $\tilde{t} = t\sqrt{g/D} = 30, 40, 50, 60, 70$. Our model is able to accurately reproduce the water surface elevation profiles for both run-up and run-down of this small amplitude solitary wave. Detailed experiment setup and additional benchmark cases are presented in Appendix A.

4.2.4 Work Flow

The core of the model is written in Fortran 95, and the parameter setup and plotting in Python 2.7 with numpy and matplotlib. The sediment module is parallelized with OpenMP. Usually at least two to three processors are used to run the simulations. Although the more processors the less time it takes, it suffers from huge diminishing return when using more than 3 processors. The hydrodynamic and sediment models are constructed as two separate modules. During each time step, the hydrodynamic module passes SWE solutions, namely the water height h and horizontal velocity u , to the sediment module. In turn, the sediment model provides feedback of updated bed elevation to the hydrodynamic module. The bed elevation updates will be reflected in changes of the source term in the SWE momentum equation, thereby affecting the flow.

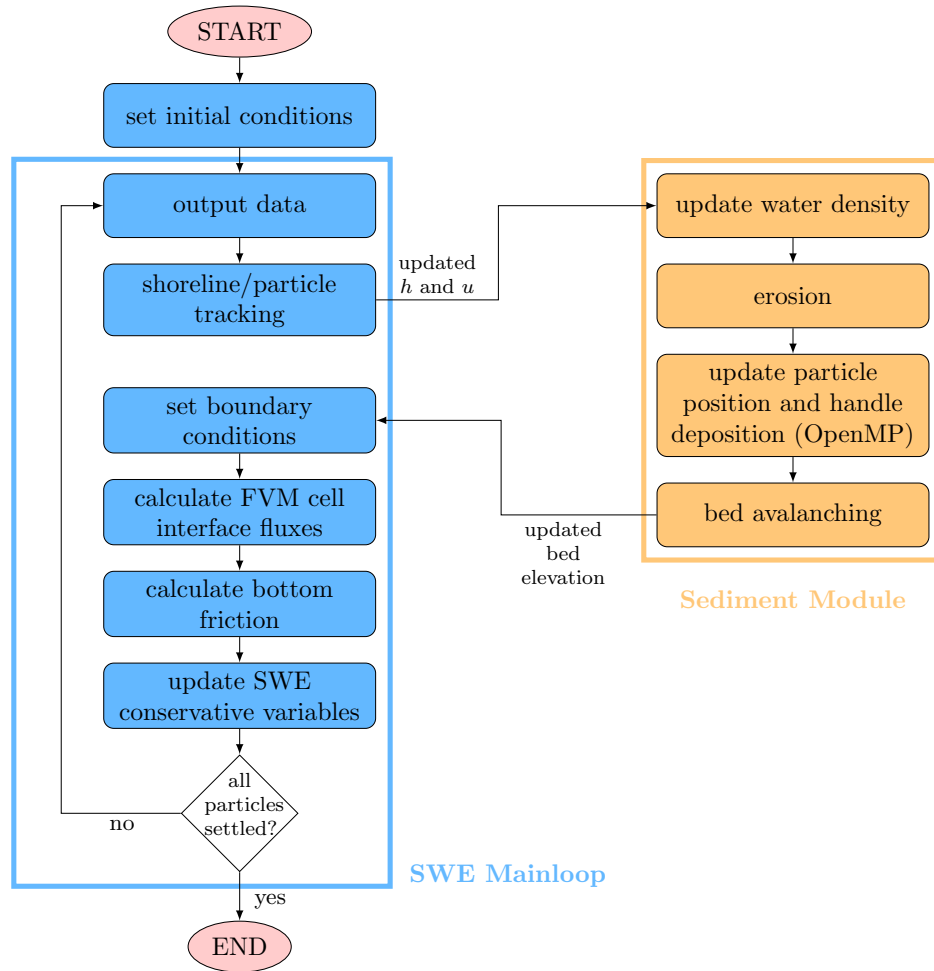


Figure 4.5: Model work flow.

4.3 Sediment Transport Validation

The MESCAPT model is applied to simulate the inundation of a tsunami similar to the 2004 Indian Ocean Tsunami and the associated sediment transport. The final result is then compared with the deposit thickness measured from Kuala Meurisi (Apostsos et al., 2011a).

Fig. 4.6a shows the initial profile. The onshore topography is comprised of a step cliff to the right and a gentle slope between the cliff and the shoreline. Fig. 4.6b shows the wave

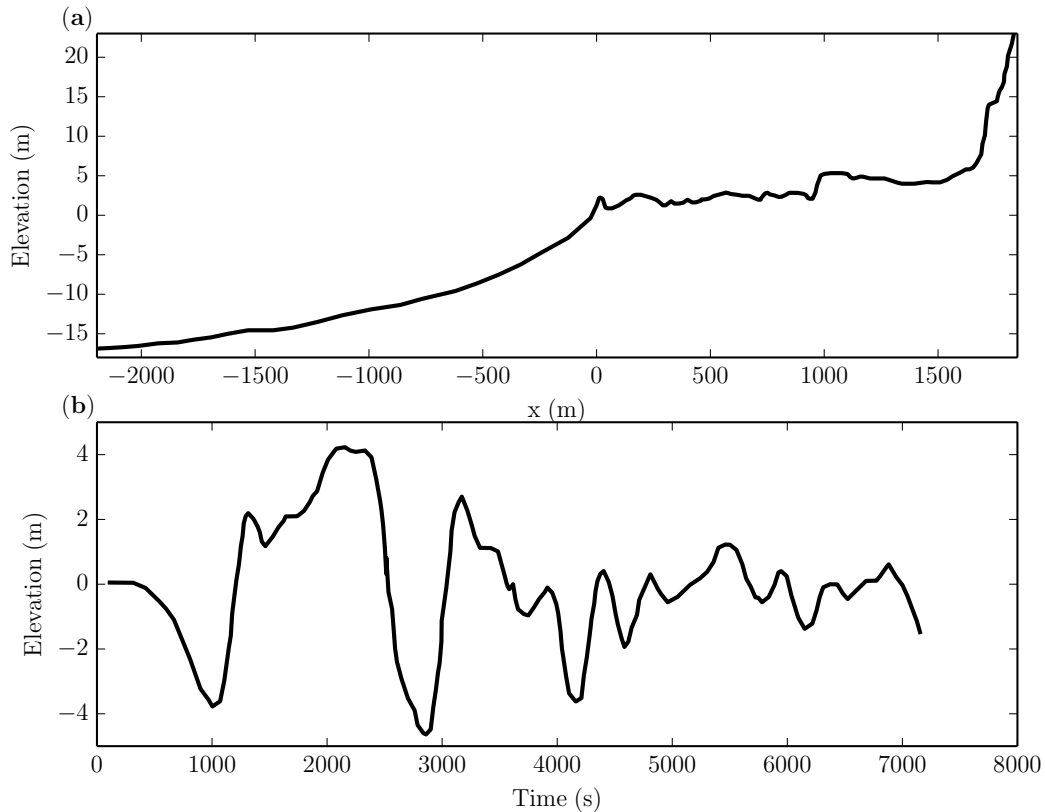


Figure 4.6: Simulation setup for the 2004 Indian Ocean Tsunami. Data are digitized from Fig. 1 in Apotsos et al. (2011a). (a) Measured topography. (b) Time series of water level in 35 m depth offshore.

boundary conditions. The near two-hour long tsunami has two main waves in the first hour. This time series of water level is predicted from a deep ocean propagation model (Apotsos et al., 2011a). The measured profile only extends to -17 m offshore, therefore we linearly extrapolated the offshore slope to -35 m to which the water level data is applicable. The extrapolation uses a slope of $1/200$, which is approximately the average slope of the offshore section seaward of -1000 m. A horizontal spacing of 10 m is used in this simulation. Initially

there is a 5 m layer of erodible sediments extending from -2000 m to the right boundary. It is assumed that there are five sediment classes with grain sizes of 0.1, 0.3, 0.5, 0.7, and 0.9 mm in equal amounts everywhere in the erodible layer.

The simulation takes approximately two days using three processors of a 3.33GHz Intel Xeon CPU. During this simulation, one meso-scale particle could contain from as few as hundreds to millions of sediment grains, depending on the instantaneous flow conditions and sediment properties where erosion occurs. Close to 20 million meso-scale particles have been generated that all deposited at the end. However, only no more than ten thousand meso-scale particles exist at any time.

The simulation results from MESCAPT is compared with both field measurements and simulation results from Apotsos et al. (2011a) (Fig. 4.7). In Fig. 4.7a, the results from MESCAPT (solid line) generally follow the trend of the simulation results by Apotsos et al. (2011a) (dashed line) using the same measured profile. While the erosion and deposition trends match relatively well between the two simulations for most locations, there are a few discrepancies. First, the magnitude of erosion depth and deposition height are larger comparing to Apotsos et al. (2011a) simulations. Second, in the vicinity of the shoreline, our simulation produced a partially submerged hump, whereas Apotsos et al. (2011a) only showed erosion. Although it is less convincing with one single data point, the left most grey circle from the field data apparently aligns with our results. In order to generate a better comparison, we picked the deposit thickness values from our simulation results where there are field measurements, and plotted them (black crosses) in Fig. 4.7b. This figure also

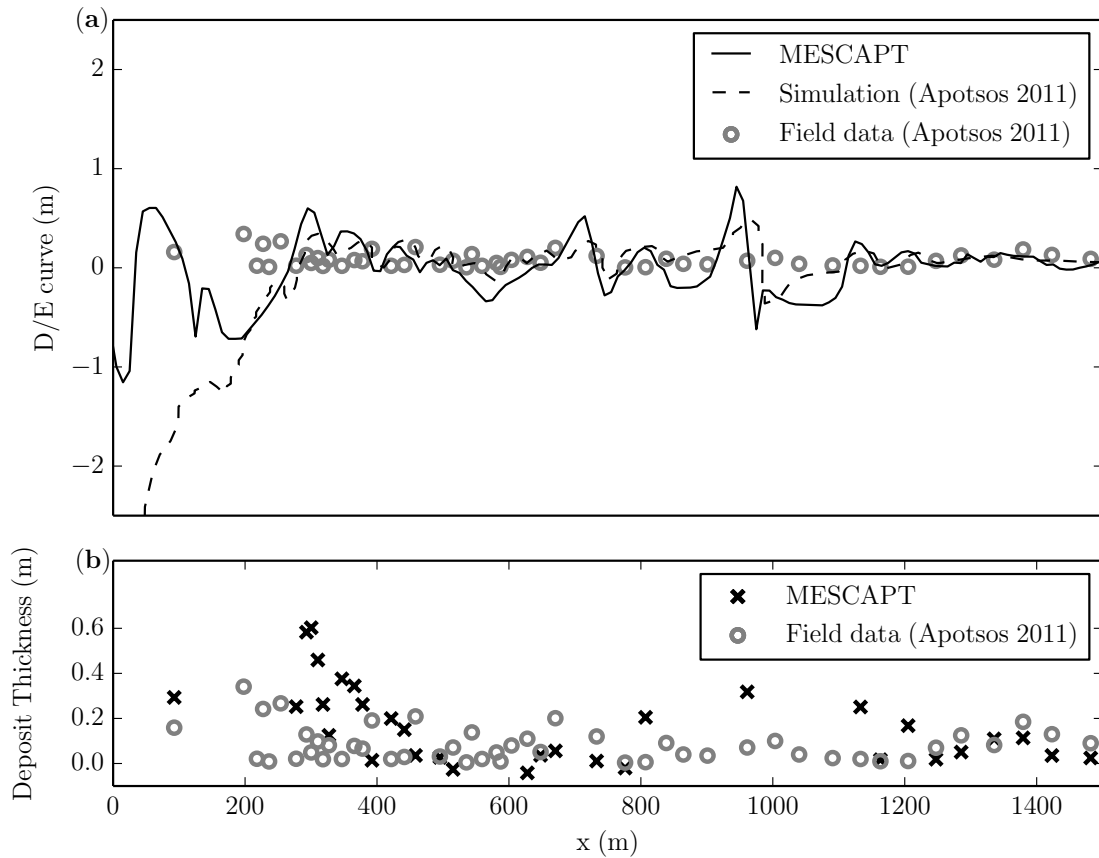


Figure 4.7: Comparison of deposition and erosion (D/E) curve between model results and field data. (a) Comparison between model results from MESCAPT (solid line) and Apotsos et al. (2011a) using measured profile (dashed line), and field data (grey circles). (b) Black crosses are the points picked from MESCAPT results where there are field measurements (grey circles).

shows that except for a few location, for example, near 600 m and 1000 m, where MESCAPT predicted erosion instead of deposition, the rest of the points are in good agreements.

Both simulation results have shown several local differences from the field measurements. The

differences can be attributed to many factors, for example, errors in the boundary waves, the initial profile, the spatial distribution and composition of sediment sources. Notably, the initial profile was surveyed after the inundation of the tsunami, which is certainly not an accurate representation of the pre-tsunami condition (Apotsos et al., 2011a). Furthermore, alongshore variations of the above factors can not be ignored, which most likely contributed to the differences between the simulated and observed deposit thicknesses. Despite the small discrepancies resulted from the aforementioned uncertainties and errors, we consider that our meso-scale method is capable of modeling sediment transport in tsunami inundation.

4.4 Model Applications

4.4.1 Model Setup and Initial Conditions

We present two idealized simulations of tsunami and storm waves running up on a single slope. The domain consists of an onshore section with a 1/100 slope and an offshore 1/20 slope (Fig. 4.8a). The horizontal spacing Δx of the hydrodynamics is 0.5 m, and the horizontal spacing of deposition grid $\Delta \xi$ is the same. Initially there is a 0.5 m thick layer of movable sand that extends from -150 m to 10 m indicated by beige color, and the dark color indicates fixed basement. The initial grain-size distribution is the same throughout the domain (Fig. 4.8b). There are four grain-size classes ranging from seven to four in ϕ scale. We simulate tsunamis as several very long solitary waves, and storms a series of shorter

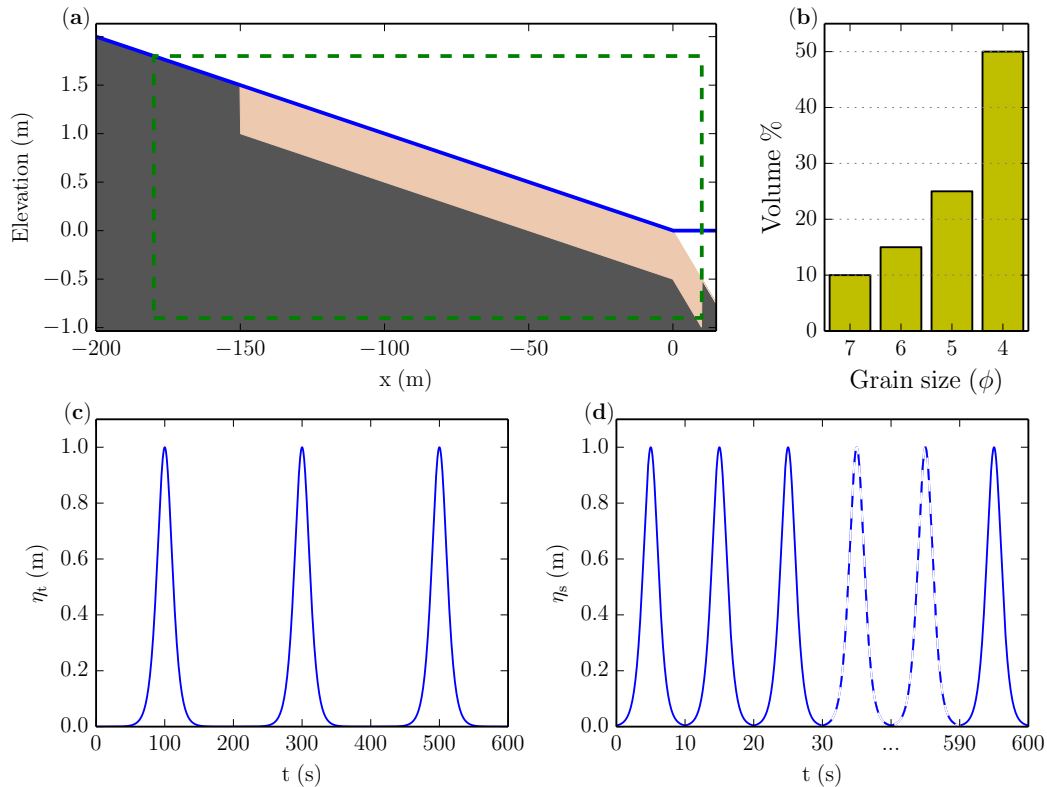


Figure 4.8: Case setup. (a) Bathymetry is composed of an onshore section with a 1 : 100 slope and an offshore 1 : 20 slope. Green dashed-line rectangle delineates the domain where sediment transport is handled. Sediment initially forms a 0.5 m thick layer that extends from -150 m to 10 m. Dark grey area that surrounds the sediment is immobile basement. (b) Bar plot of initial grain-size distribution. Grain size is in ϕ scale. For this case, a positively-skewed distribution is used, and the coarsest fraction is 50%. (c) and (d) show right boundary conditions. Tsunami waves have a period of 200 s, and storm waves 10 s. They both have initial wave heights of 1 m.

period waves, which allows simple parametric wave setup. Fig. 4.8c and Fig. 4.8d show the wave boundary conditions of 200-second-period tsunami waves and 10-second-period storm

waves that both last 600 s. The wave heights are both 1 m. The two types of wave both enter the domain from the right boundary starting from the beginning of each simulation.

4.4.2 Results

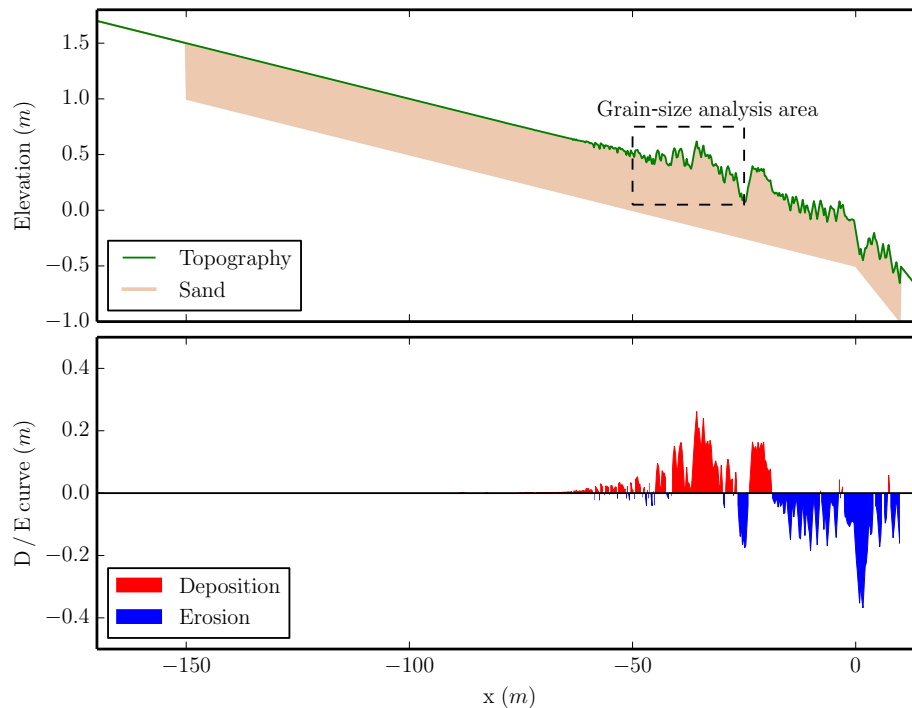


Figure 4.9: Storm simulation results. The top pane shows the sand bed surface elevation at end of the storm simulation. The dashed line delineates where a grain-size analysis is performed (Fig. 4.11). The bottom pane shows the deposition-erosion curve, where positive denotes deposition and negative erosion, in comparison with the original bed elevation.

Both simulations last 1000 s, at the end of which all sediment particles have settled down.

Fig. 4.9 and Fig. 4.10 show the morphological changes of the storm and tsunami case

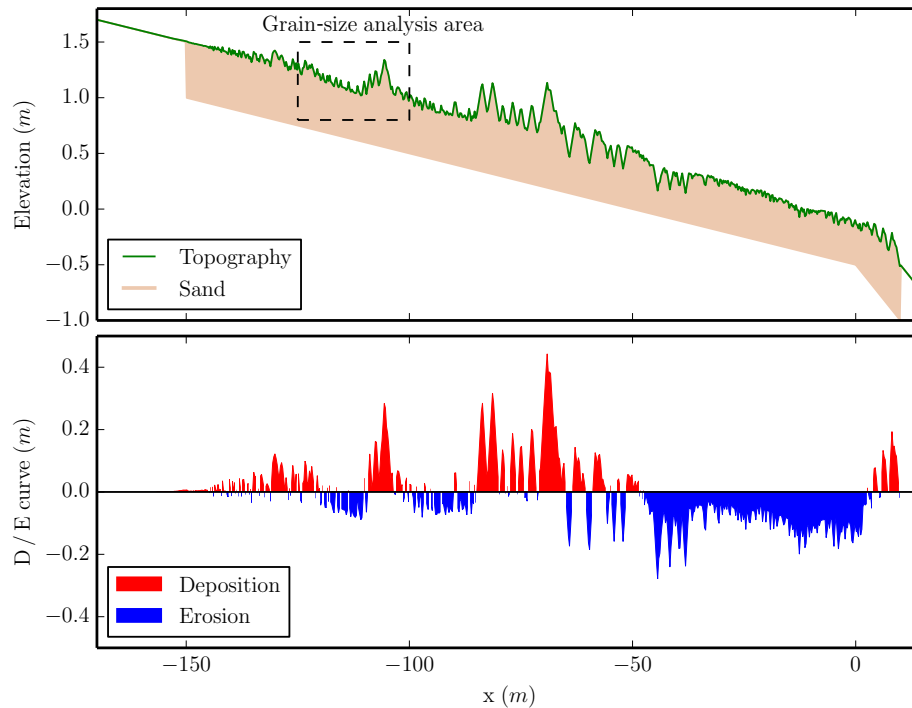


Figure 4.10: Tsunami simulation results. The configuration is the same as Fig. 4.9.

respectively.

The most striking difference between the two simulations is that tsunami deposits reach much farther inland than storm deposits. Tsunami deposits extend beyond 150 m inland, while storm deposits only a little over 60 m. Another more subtle difference lies in their offshore morphological changes. The offshore changes of the storm case is dominated by erosion, indicated by blue color in Fig. 4.9. In contrast, tsunami leaves behind deposits offshore. The reason behind the above is, unsurprisingly, due to the differences between the hydrodynamics of the storm and tsunami waves, since this is the only different aspect of the two cases. Each tsunami wave has a period of 200 s, and each storm wave is only

1/20 as long. Therefore the tsunami inundates much farther than the storm and creates more erosion and deposition. In addition, the tsunami also generates strong return flows, which is not seen in the storm case. This explains why the tsunami leaves offshore deposits and storm doesn't. Despite the huge distinction between the two events, there exist a few similarities. Both deposits can be roughly divided into an erosion zone closer to the shore and a deposition zone beyond, except that the tsunami erosion zone is wider. Also, both deposits taper landward.

In addition to predicting the general morphological features of storm and tsunami deposits, the strength of this model is the capability of producing detailed deposit structure. We present the analysis of the storm deposits in Fig. 4.11. The area ranges from -50 m to -25 m horizontally, covering most of the storm deposition area. Two horizontal sampling densities are chosen, one Δx per 2.5 m and one Δx per 1.25 m, shown in the top and bottom pane, respectively. All the columns in the top pane can be found in the bottom with matching horizontal positions. Each column plots the grain-size distribution and the trend of the median diameter (d_{50}) of each layer within a single horizontal spacing Δx . The percentage of each sediment class within a layer is denoted by a color-coded rectangle, and the d_{50} trend is plotted with connect yellow dots. The columns are showing the movable bed thickness instead of elevation, i.e., the base of the movable bed is leveled to the same elevation. Across all the columns, the red and blue curve indicate the upper and lower bounds of the event deposits. Finally, the void above the top layer is padded with the initial grain-size distribution in order to mimic sandwiched event deposits in the geological record.

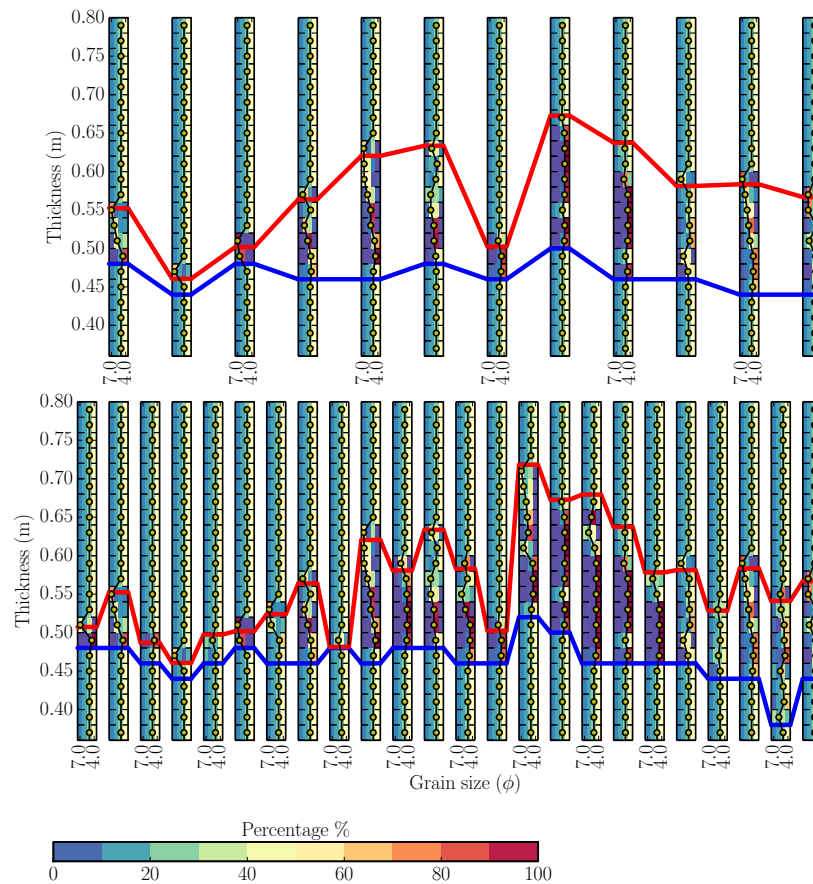


Figure 4.11: Comparison of grain-size analysis plots between different sampling density for the idealized storm case. The area of interest is delineated with dashed lines in Fig. 4.9. The top pane uses a sampling density of one Δx per 2.5 m, while the bottom doubles the density. The top columns are aligned with the same column in the bottom. Each column shows the grain-size distribution and d_{50} trend of the deposition layers. The percentage of each sediment class within a layer is denoted by a color-coded rectangle. A black curve with yellow dots connecting all the layers shows the d_{50} trend. The columns are showing the thickness of the movable bed instead of the elevation.

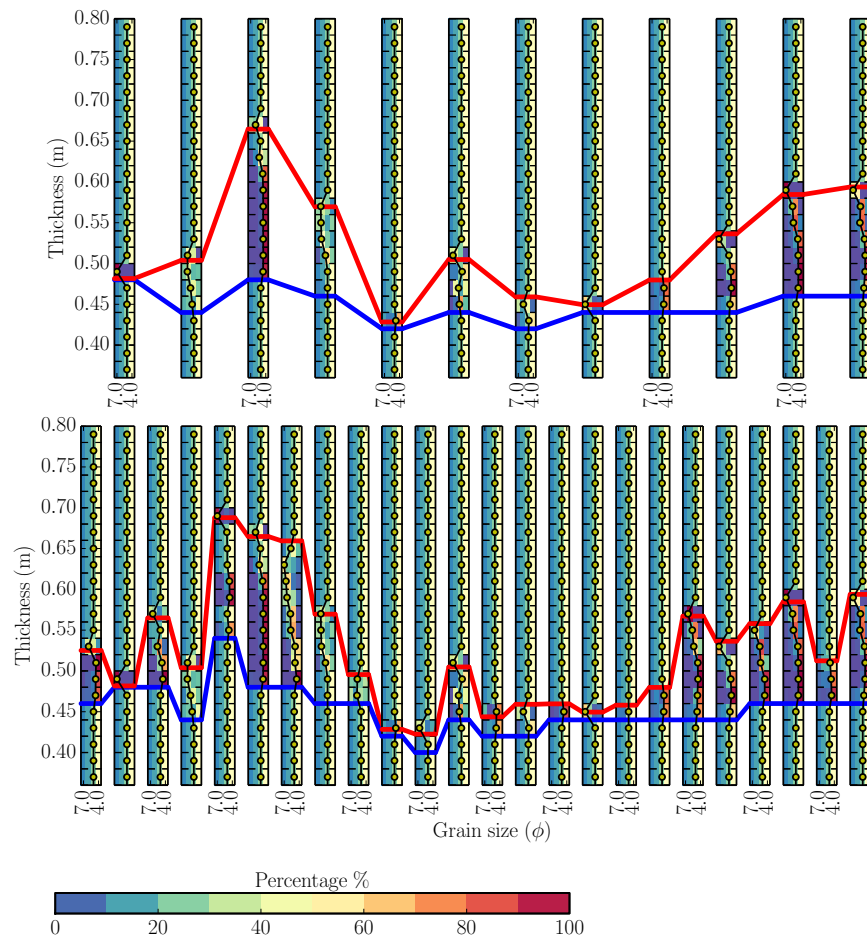


Figure 4.12: Comparison of grain-size analysis plots between different sampling density for the idealized tsunami case. The area of interest is delineated with dashed lines in Fig. 4.10. The top pane uses a sampling density of one Δx per 2.5 m, while the bottom doubles the density. Refer to the caption of Fig. 4.11 for definition of colors and curves.

The grain-size distribution analysis reveals the overall fining inland and fining upward trend of the storm deposits. Similarly, Fig. 4.12 also shows fining inland and upward trends for the tsunami case. More importantly, by comparing the results from two different sampling densities, it demonstrates that the lower the sampling density, the less information we can

extract from the samples, or the larger the error. The error can be defined as the normalized difference of, for example, deposit thickness between interpolated results from sampling and raw model output. Therefore this model might help reveal an optimal sampling density as a function of, say, wave height, onshore slope, and grain-size distribution, via parameter study.

4.4.3 Discussion

The deposits and erosion (Fig. 4.9 and 4.10) from both tsunami and storm cases are rich in detail, and more complicated comparing to previous simulation results. For example, the linear profile case from Apotsos et al. (2011a), which also have simple two-slope setup for the initial profile, only produces smooth deposits despite having more complicated wave series. This indicates there are fundamental differences between the particle approach and the concentration approach. Particle-based methods can produce more detailed sediment transport and deposits. However, whether or not the increase in detail is equivalent to increase in accuracy still remains a question. Current field data sampling approach doesn't allow comparison with such detailed deposit pattern due to the coarse sampling spacing. Another issue for field data is preservation, tsunami deposits are very vulnerable to the various coastal processes, therefore paleotsunami deposits are most likely different from their original state (Goto et al., 2014).

While the ultimate goal of the MESCAPT model is to study the similarities and differences between tsunami and storm deposits, it is beyond the scope of this paper. The two idealized

cases are far from enough to arrive at any conclusions on this complicated subject. Rather, the cases in this paper serve as a demonstration of the capabilities of the model. To approach the problem of comparison between the two types of event deposits, a systematic parameter study needs to be conducted to quantify how different aspects of the two events affect the results.

4.5 Model Limitations and Potential Future Directions

The MESCAPT model has shown its capability of simulating the sediment transport of a tsunami similar to the 2004 Indian Ocean Tsunami, and producing general grain size trends in the idealized case studies. However, there are many limitations in the current model. First and foremost, currently the model is only one dimensional in the horizontal direction. In many cases where a tsunami or storm approaches the shore at a angle, longshore current and sediment transport cannot be ignored. Besides, the longshore variations in the initial bathymetry and topography could also impact the hydrodynamics and sediment transport. Extending to two dimensions horizontally also allows the integration of full turbulence hydrodynamic models. Secondly, the hydrodynamic model is simplistic. The hydrodynamic model uses the depth-average NSWE and then calculates the velocity profile. This approach results in great computational efficiency at the cost of accuracy. Coupling with a 3D turbulence model, such as RANS, LES, DNS, or SPH, would significantly improve model accuracy, provided the meso-scale particle transport model is also extended to 3D.

In terms of the computational method and efficiency, the current model can only utilize one computer, or a single node in a supercomputer. OpenMP is implemented for the particle calculations so that multiple processors can run at the same time to increase efficiency. A potentially better alternative is Message Passing Interface (MPI), which can distribute the computational load into different nodes. Another issue with the current version of MESCAPT is that the horizontal spacing Δx is constant. For simulation domains that contain a long offshore component this is very inefficient when the focus is on onshore sediment transport. In these scenarios, it is ideal to use a variable Δx . Δx can be set larger for offshore areas and where topography gradient is small.

For storm simulations, the waves are too much simplified. More realistic storm waves should have a spectrum of wave periods and varying wave height. For example, the SWAN spectral wave model can be integrated to simulate the evolution of the spectrum of wind-driven waves in storms. Also storm usually has a surge component, which is not included in the simulations.

Factors that are not modeled that could affect the results and interpretation include, vegetation effect, non-uniform manning's coefficient, post depositional changes, among others.

4.6 Conclusions

We presented a model for erosion, transport and deposition of sediment during tsunamis and storms that is based on meso-scale particles. While our meso-scale model can be coupled with

any hydrodynamic model, we coupled it with a model based on the Shallow Water equations. The hydrodynamic model showed excellent agreement with established benchmark cases. The coupled model was applied to simulate a tsunami similar to 2004 Indian Ocean Tsunami, and the results compared well with field measurements. The results from idealized storm and tsunami simulations indicated that our meso-scale model is capable of reproducing macroscopic characteristics of tsunami and storm deposits, such as landward thinning, as well as landward and upward fining of the grain-size distribution. The main advantage of our meso-scale model, however, is that it is capable of reproducing the internal stratigraphy of deposits. One possible application of our model is to assist and evaluate field-based methods. We presented an example that showed how the inferred thickness distribution varies as a function of samples along the the runup. This example also demonstrates how complicated tsunami and storm deposits are, given that we assumed a simple slope as initial condition. The meso-scale concept is a paradigm that bridges the gap between being able to consider sediment transport and reproduce stratigraphy on geophysically relevant spatial and temporal scales. Because this concept allows us to simulate sediment dynamics during storms and tsunamis, no matter if grains are moved in suspension or bed load, in a consistent modeling framework, perhaps similarities or more importantly differences in how storm and tsunamis move sediment can be quantitatively and systematically studied and so help to distinguish between storm and tsunami deposits in the geologic record where both causative events are competing natural hazards.

Notation

Table 4.1: Notation

F	force.
V	volume.
ρ	density.
u	horizontal velocity.
v	vertical velocity.
g	gravitational acceleration.
C_{drag}	drag coefficient.
r	radius.
Δz_b	bed sliding flux.
S_{wet}	submerged critical slope.
\dot{z}_{max}	maximum bed sliding rate.
$\Delta \xi$	deposition column width.
Δx	step size in space.
Δt	step size in time.
ω_i	volumetric pickup rate of i th grain-size class.
Δ	$(\rho_s - \rho_f) / \rho_f$.
d_{50}	median grain size.
ν	kinematic viscosity.

u_*	shear velocity.
$u_{*,cr}$	Shields critical shear velocity.
h_b	bedload layer height.
u'_{rms}, v'_{rms}	RMS values of horizontal and vertical velocity fluctuations.
k	turbulence kinetic energy in k - ε model.
ε	dissipation in k - ε model.
τ_e	eddy lifetime.
u_e, v_e	eddy velocities.
L_e	eddy radius.
N_u, N_v	random numbers.
h	water depth.
f	friction.
n	Manning coefficient.
$()_s$	sediment.
$()_f$	fluid.
$()_\alpha$	reference level.
$()'$	fluctuations.
$()^+$	wall non-dimensionalized.

Acknowledgement

This publication is dedicated to H. Richard (Rich) Lane (1942 - 2015), director of the Sedimentary Geology and Paleobiology Program at NSF. Thanks for your support, Rich. You will be missed. The work presented in here is based upon work partially supported by the National Science Foundation under grants NSF-CMMI-1208147, NSF-CMMI-1206271, NSF-EAR-1312813, and NSF-EAR-1136534.

Chapter 5

Future Work

This chapter mainly discusses the future work of the MESCAPT model. The shallow water hydrodynamic model was validated against several experimental and analytical data, and the meso-scale particle model was validated via simulating the sediment transport of a tsunami similar to the 2004 Indian Ocean Tsunami, and producing general grain size trends in the idealized case studies. However, as is shown in Section 4.5, the model still have many limitations, therefore we propose the following improvements of the model.

First, extending the model from one dimensional to two dimensional for the hydrodynamics, if a shallow water model is still used. Alternatively, use a three dimensional turbulence model such as RANS or LES. In either case, the sediment transport model needs to be extended to three dimensional. In fact, the current version of the meso-scale particle model was initially developed with 3D in mind. The naming of variables and construction of arrays

and algorithms made it easy to be adapted to 3D. With this change, it will be possible to model more realistic tsunami and storm conditions, for example, when the incoming wave is not perpendicular to the shoreline, which could generate significant longshore sediment transport. Also, the initial profile and sediment composition and distribution variations alongshore will be able to be considered.

The proposed increase in dimension could greatly impact computation time, especially for three dimensional turbulence models. OpenMP, which is employed in the current sediment transport model, may not be sufficient. A better method is Message Passing Interface (MPI). With MPI, the computational domain is decomposed into several smaller domains, and the work load for each domain is distributed to a network of computers, or to different nodes in the case of a supercomputer.

The constant horizontal grid spacing should be changed to variable. For example, in the case of the sediment transport validation in Section 4.3, in order to propagate the tsunami waves from -33 m water depth offshore, we used an offshore distance of over 2000 m, and an onshore distance of 1800 m. The grid spacing is the same everywhere, which is inefficient because our interest for this case is mostly onshore, not offshore. With variable grid spacing implemented, we could coarsen the grid where local variations of topography or bathymetry is small, or where there is no research interests. On the other hand, we could reduce the grid spacing where we need high resolution results.

In order for the storm simulation to be more realistic, we need to model the storm wave spectrum and storm surge. For example, the SWAN spectral wave model can be coupled to

the shallow water model to simulate the evolution of the spectrum of wind-driven waves in storms. For storm surge, we could either use a simple sine function for idealized studies, or empirical equations for specific field locations (e.g., Xu and Huang, 2014).

Currently, the MESCAPT model can only handle sandy sediment. Cohesive sediment, such as mud, is also an important component of tsunami deposits. For instance, Abe et al. (2012) reported that tsunami deposits evolve from sand to sand-dominated to mud dominated in the landward direction for the 2011 Japan tsunami. By incorporating cohesive sediment transport, we could potentially reproduce rip-up mud clasts typically found in tsunami deposits. However, the complex processes of cohesive sediment transport, such as flocculation and consolidation, are still not well understood. Modeling cohesive sediment could also require knowledge of the geochemical and biological properties of the sediment for the erosion and transport (Grabowski et al., 2011). Moreover, how the current understanding of cohesive transport can be translated into particles and even meso-scale particles poses great challenge.

With the above improvements implemented, to approach the ultimate goal of studying the similarities and differences between tsunamis and storms, we need to conduct a systematic parameter study to quantify the influence of individual parameter on different aspects of the final results and the sediment transport process.

The application of MESCAPT need not be limited to tsunami and storm sediment transport. This model can also be applied to study riverine sandy sediment transport. After all, the pick-up function employed in MESCAPT was initially developed in a flume experiment (van Rijn, 1984) that resembles a river environment. Some preliminary features for riverine

sediment transport has been implemented, such as periodic boundary conditions for sediment particles to simulate sediment transport in steady flow over a long period of time. Other applications may include simulating the sequences in river delta systems.

Bibliography

- Abe, T., Goto, K., and Sugawara, D. (2012). Relationship between the maximum extent of tsunami sand and the inundation limit of the 2011 Tohoku-oki tsunami on the Sendai Plain, Japan. *Sedimentary Geology*, doi:10.1016/j.sedgeo.2012.05.004.
- Apotsos, A., Gelfenbaum, G., and Jaffe, B. (2011a). Process-based modeling of tsunami inundation and sediment transport. *Journal of Geophysical Research: Earth Surface (2003–2012)*, 116(F1).
- Apotsos, A., Gelfenbaum, G., and Jaffe, B. (2012). Time-dependent onshore tsunami response. *Coastal Engineering*, 64:73–86.
- Apotsos, A., Gelfenbaum, G., Jaffe, B., Watt, S., Peck, B., Buckley, M., and Stevens, A. (2011b). Tsunami inundation and sediment transport in a sediment-limited embayment on american samoa. *Earth Science Reviews*, accepted.
- Atwater, B., ten Brink, U., Buckley, M., Halley, R., Jaffe, B., Lopez-Venegas, A., Reinhardt, E., Tuttle, M., Watt, S., and Wei, Y. (2012). Geomorphic and stratigraphic evidence for

- an unusual tsunami or storm a few centuries ago at anegada, british virgin islands. *Natural Hazards*, 63:51–84.
- Bahlburg, H. and Weiss, R. (2007). Sedimentology of the December 26, 2004, Sumatra Tsunami deposits in intermediate and large distances, Eastern India (Tamil Nadu) and Kenya. *International Journal of Earth Sciences*, 96:1195–1209.
- Bondevik, S. (2008). The sands of tsunami time. *Nature*, 455(7217):1183–4.
- Bourgeois, J. (2009). Geologic effects and records of tsunamis. In Bernard, E. and Robinson, A., editors, *The Sea: Tsunamis*, volume 15, pages 55–91. Harvard University Press.
- Bozzi, S. and Passoni, G. (2012). Mathematical modelling of bottom evolution by particle deposition and resuspension. *Applied Mathematical Modelling*, 36(9):4186–4196.
- Calantoni, J., Holland, K. T., and Drake, T. G. (2004). Modelling sheet-flow sediment transport in wave-bottom boundary layers using discrete-element modelling. *PHILOSOPHICAL TRANSACTIONS-ROYAL SOCIETY OF LONDON SERIES A MATHEMATICAL PHYSICAL AND ENGINEERING SCIENCES*, 362:1987–2002.
- Castro, M. J., Ferreiro, A. F., García-Rodríguez, J. A., González-Vida, J. M., Macías, J., Parés, C., and Vázquez-Cendón, M. E. (2005). The numerical treatment of wet/dry fronts in shallow flows: application to one-layer and two-layer systems. *Mathematical and Computer Modelling*, 42(3):419–439.
- Choowong, M., Murakoshi, N., Hisada, K.-i., Charusiri, P., Charoentitirat, T.,

- Chutakositkanon, V., Jankaew, K., Kanjanapayont, P., and Phantuwongraj, S. (2008). 2004 indian ocean tsunami inflow and outflow at phuket, thailand. *Marine Geology*, 248(3):179–192.
- Cooper, J. R., Wainwright, J., Parsons, A. J., Onda, Y., Fukuwara, T., Obana, E., Kitchener, B., Long, E. J., and Hargrave, G. H. (2012). A new approach for simulating the redistribution of soil particles by water erosion: A marker-in-cell model. *Journal of Geophysical Research: Earth Surface (2003–2012)*, 117(F4).
- Dawson, A. G. and Shi, S. (2000). Tsunami deposits. *Pure and applied geophysics*, 157(6-8):875–897.
- Delis, A. I., Kazolea, M., and Kampanis, N. A. (2008). A robust high-resolution finite volume scheme for the simulation of long waves over complex domains. *International Journal for Numerical Methods in Fluids*, 56(4):419–452.
- Evans, M. W., Harlow, F. H., and Bromberg, E. (1957). The particle-in-cell method for hydrodynamic calculations. Technical report, DTIC Document.
- Goff, J., Chague-Goff, C., Nichol, S., Jaffe, B., and Dominey-Howes, D. (2012). Progress in Paleotsunami Research. *Sedimentary Geology*, 243–244:70–88.
- Goff, J., McFadgen, B., and Chague-Goff, C. (2004). Sedimentary differences between the 2002 eastern storm and the 15th-century okoropunga tsunami southeastern north island, new zealand. *Marine Geology*, 204:235–250.

- Goto, K., Chague-Goff, C., Fujiro, S., Jaffe, B., Nishimura, Y., Richmond, B., Sugawara, D., Szczucinski, W., Tappin, D., Witter, R., and Yulianto, E. (2011). New insights of tsunami hazard from the 2011 tohoku-oki event. *Marine Geology*, 290(1–4):46–50.
- Goto, K., Ikehara, K., Goff, J., Chagué-Goff, C., and Jaffe, B. (2014). The 2011 tohoku-oki tsunamithree years on. *Marine Geology*, 358:2–11.
- Grabowski, R. C., Droppo, I. G., and Wharton, G. (2011). Erodibility of cohesive sediment: the importance of sediment properties. *Earth-Science Reviews*, 105(3):101–120.
- Graham, D. and James, P. (1996). Turbulent dispersion of particles using eddy interaction models. *International Journal of Multiphase Flow*, 22(1):157–175.
- Hindson, R., Andrade, C., and Dawson, A. (1996). Sedimentary processes associated with the tsunami generated by the 1755 lisbon earthquake on the algarve coast, portugal. *Physics and Chemistry of the Earth*, 21(1):57–63.
- Hinze, J. (1975). Turbulencemcgraw-hill. *New York*, 218.
- Huntington, K., Bourgeois, J., Gelfenbaum, G., Lynett, P., Jaffe, B., Yeh, H., and Weiss, R. (2007). Sandy signs of a tsunami’s onshore depth and speed. *Eos*, 88(52):577–578.
- Jaffe, B. (2008). The role of deposits in tsunami risk assessment. In *Solutions to Coastal Disasters 2008@ sTsunamis*, pages 256–267. ASCE.
- Jaffe, B. and Gelfenbaum, G. (2007). A simple model for calculating tsunami flow speed from tsunami deposits. *Sedimentary Geology*, 200:347–361.

Jankaew, K., Atwater, B. F., Sawai, Y., Choowong, M., Charoentitirat, T., Martin, M., and Prendergast, A. (2008). Medieval forewarning of the 2004 Indian Ocean tsunami in Thailand. *Nature*, 455:1228–1231.

Johnson, B. H. (1974). Investigation of mathematical models for the physical fate prediction of dredged material. Technical report, DTIC Document.

Kanamori, H. (1977). The energy release of great earthquakes. *Journal of Geophysical Research*, 82:2981–2987.

Kortekaas, S. and Dawson, A. (2007). Distinguishing tsunami and storm deposits: an example from martinhal, sw portugal. *Sedimentary Geology*, 200(3):208–221.

Kraus, N. C. and Wamsley, T. V. (2003). Coastal barrier breaching. part 1. overview of breaching processes. Technical report, DTIC Document.

Lange, R. (1973). A three-dimensional computer code for the study of pollutant dispersal and deposition under complex conditions. *Lawrence Livermore Laboratory report UCRL-51462*.

Lange, R. and Knox, J. (1974). Adaptation of a three-dimensional atmospheric transport-diffusion model to rainout assessments. Technical report, California Univ., Livermore (USA). Lawrence Livermore Lab.

Liu, B. Y. and Agarwal, J. K. (1974). Experimental observation of aerosol deposition in turbulent flow. *Journal of Aerosol Science*, 5(2):145–155.

- Liu, P. L.-F., Lynett, P., and Synolakis, C. E. (2003). Analytical solutions for forced long waves on a sloping beach. *Journal of Fluid Mechanics*, 478:101–109.
- MacInnes, B., Weiss, R., Bourgeois, J., and Pinegina, T. (2010). Slip Distribution of the 1952 Kamchatka Great Earthquake Based on Near-Field Tsunami Deposits and Historical Records. *Bulletin of the Seismological Society of America*, 100(4):1695–1709.
- Martin, M. E., Weiss, R., Bourgeois, J., Pinegina, T. K., Houston, H., and Titov, V. V. (2008). Combining constraints from tsunami modeling and sedimentology to untangle the 1969 Ozernoi and 1971 Kamchatskii tsunamis. *Geophysical Research Letters*, 35:L01610.
- Matida, E. A., Nishino, K., and Torii, K. (2000). Statistical simulation of particle deposition on the wall from turbulent dispersed pipe flow. *International Journal of Heat and Fluid Flow*, 21(4):389 – 402.
- McCall, R., De Vries, J. V. T., Plant, N., Van Dongeren, A., Roelvink, J., Thompson, D., and Reniers, A. (2010). Two-dimensional time dependent hurricane overwash and erosion modeling at santa rosa island. *Coastal Engineering*, 57(7):668–683.
- Middleton, G., Church, M. J., Coniglio, M., Hardie, L. A., and Longstaffe, F. J. (2003). *Encyclopaedia of Sediments and Sedimentary Rocks*. Kluwer Academic Publishers, Dordrecht.
- Minoura, K., Imamura, F., Sugawara, D., Kono, Y., and Iwashita, T. (2001). The 869 Jogan tsunami deposit and recurrence interval of large-scale tsunami on the Pacific coast of northeastern Japan. *Journal of Natural Disaster Science*, 23:83–88.

- Minoura, K. and Nakaya, S. (1991). Traces of tsunami preserved in teh inter-tidal lacustrine and marsh deposits: some examples form northeastern Japan. *Journal of Geology*, 99:265–287.
- Morrison, F. (2013). *An Introduction to Fluid Mechanics*. Cambridge University Press.
- Morton, R. A., Gelfenbaum, G., and Jaffe, B. (2007). Physical criteria for distinguishing sandy tsunami and storm deposits using modern examples. *Sedimentary Geology*, 200:184–207.
- Namegaya, Y., Satake, K., and Yamaki, S. (2010). Numerical simulation of the AD Jogan tsunami in Ishinomaki and Sendai plains and Ukedo river-mouth. *Annual Report of Active Fault and Paleearthquake Research*, 10:1–21.
- Nanayama, F. and Shigeno, K. (2006). Inflow and outflow facies from the 1993 tsunami in southwest hokkaido. *Sedimentary Geology*, 187(3):139–158.
- Nanayama, F., Shigeno, K., Satake, K., Shimokawa, K., Koitabashi, S., S., M., and Ishii, M. (2000). Sedimentary differences between the 1993 Hokkaido–Nansei–Oki tsunami and the 1959 Miykojima typhoon at Taisei southwestern Hokkaido, northern Japan. *Sedimentary Geology*, 135:255–264.
- Nwogu, O. (1993). Alternative form of boussinesq equations for nearshore wave propagation. *Journal of Waterway, Port, Coastal, and Ocean Engineering*, 119(6):618–638.
- Parry, M. L. (2007). *Climate Change 2007: impacts, adaptation and vulnerability: contribu-*

- tion of Working Group II to the fourth assessment report of the Intergovernmental Panel on Climate Change*, volume 4. Cambridge University Press.
- Roe, P. (1997). Approximate riemann solvers, parameter vectors, and difference schemes. *Journal of Computational Physics*, 135(2):250 – 258.
- Roelvink, D., Reniers, A., van Dongeren, A., van Thiel de Vries, J., McCall, R., and Lescinski, J. (2009). Modelling storm impacts on beaches, dunes and barrier islands. *Coastal Engineering*, 56(11):1133–1152.
- Satake, K., Namegaya, Y., and Yamaki, S. (2008). Numerical simulation of the AD Jogan tsunami in Ishinomaki and Sendai plains. *Annual Report of Active Fault and Paleoseismic Research*, 8:71–81.
- Schlichting, H., Gersten, K., and Gersten, K. (2000). *Boundary-layer theory*. Springer Science & Business Media.
- Sitanggang, K. I. and Lynett, P. J. (2010). Multi-scale simulation with a hybrid boussinesq-rans hydrodynamic model. *International Journal for Numerical Methods in Fluids*, 62(9):1013–1046.
- Smith, J. and McLean, S. (1977). Spatially averaged flow over a wavy surface. *Journal of Geophysical Research*, 82(2):1735–1746.
- Spaulding, M. L. and Pavish, D. (1984). A three-dimensional numerical model of particulate transport for coastal waters. *Continental Shelf Research*, 3(1):55–67.

- Spinewine, B., Capart, H., Le Grelle, N., Soares Frazão, S., and Zech, Y. (2002). Experiments and computations of bankline retreat due to geomorphic dam-break floods. In *Proceedings of River flow*, pages 651–661.
- Spiske, M., Weiss, R., Roskosch, J., and Bahlburg, H. (2008). Inversion of flow depth and speed from tsunami deposits using TsuSedMod. *Eos Trans. AGU, Fall Meet. Suppl.*, 89(52):OS53A–1288.
- Sugawara, D., Imamura, F., Matsumoto, T., Goto, K., and Minoura, K. (2011). Reconstruction of the AD 869 Jogan earthquake induced tsunami by using geologic data. *Journal of Natural Disaster Science*, 29:501–516.
- Synolakis, C. (1986). *The runup of long waves*. PhD thesis, California Institute of Technology.
- Synolakis, C. (1987). The runup of solitary waves. *J. Fluid Mech.*, 185:523–545.
- Synolakis, C., Bernard, E., Titov, V., Kanoglu, U., and Gonzalez, F. I. (2008). Validation and verification of tsunami numerical models. *Pure Appl. Geophys.*, 165(11–12):2197–2228.
- Szczucinski, W. (2012). The post-depositional changes of the onshore 2004 tsunami deposits on the Andaman Sea coast of Thailand. *Natural Hazards*, 60:115–133.
- Titov, V. and Synolakis, C. (1998). Numerical modeling of tidal wave runup. *Journal of Waterway, Port, Coastal and Ocean Engineering*, 124(4):157–171.
- Titov, V. and Synolakis, C. (1995). Modeling of breaking and nonbreaking long-wave evolu-

- tion and runup using VTSC-2. *Journal of Waterway, Port, Coastal and Ocean Engineering*, 121(308–316).
- Tuck, E. and Hwang, L.-S. (1972). Long wave generation on a sloping beach. *Journal of Fluid Mechanics*, 51(03):449–461.
- Tuttle, M. P., Ruffman, A., Anderson, T., and Jeter, H. (2004). Distinguishing tsunami from storm deposits in eastern north america: the 1929 grand banks tsunami versus the 1991 halloween storm. *Seismological Research Letters*, 75(1):117–131.
- Van Dongeren, A., Lowe, R., Pomeroy, A., Trang, D. M., Roelvink, D., Symonds, G., and Ranasinghe, R. (2013). Numerical modeling of low-frequency wave dynamics over a fringing coral reef. *Coastal Engineering*, 73:178–190.
- van Rijn, L. C. (1984). Sediment pick-up functions. *Journal of Hydraulic Engineering*, 110(10):1494–1502.
- Wei, G., Kirby, J. T., Grilli, S. T., and Subramanya, R. (1995). A fully nonlinear boussinesq model for surface waves. part 1. highly nonlinear unsteady waves. *Journal of Fluid Mechanics*, 294:71–92.
- Wei, Y., Bernard, E., Tang, L., Weiss, R., Titov, V., Moore, C., Spillane, M., M., H., and Kanoglu, U. (2008). Real-time experimental forecast of the Peruvian tsunami of August 2007 for U.S. coastlines. *Geophysical Research*, 35:L04609.

- Weiss, R. (2008). Sediment grains moved by passing tsunami waves: Tsunami deposits in deep water. *Marine Geology*, 250:251–257.
- Wiberg, P. and Smith, J. (1989). A theoretical model for saltating grains in water. *Journal of Geophysical Research*, 90:7341–7354.
- Wiberg, P. L. and Smith, J. D. (1985). Model for calculating bed load transport of sediment. *Journal of Hydraulic Engineering*, 115(1):101–123.
- Witter, R., Jaffe, B., Zhang, Y., and Priest, G. (2011). Reconstructing hydrodynamic flow parameters of the 1700 tsunami at Cannon Beach, Oregon, U.S.A. *Natural Hazards*, DOI: 10.1007/s11069-011-9912-7.
- Wu, W. (2004). Depth-averaged two-dimensional numerical modeling of unsteady flow and nonuniform sediment transport in open channels. *Journal of hydraulic engineering*, 130(10):1013–1024.
- Xu, S. and Huang, W. (2014). An improved empirical equation for storm surge hydrographs in the gulf of mexico, usa. *Ocean Engineering*, 75:174–179.

Appendix A

Hydrodynamic Model Validation

Three additional cases are presented in this section for validating the SWE hydrodynamic model.

A.1 Solitary Wave Running Up on A Canonical Beach

(continued)

Synolakis (1987) performed a series of experiments with solitary waves running up on a canonical beach in a wave tank at California Institute of Technology, Pasadena. The wave tank consists of a constant-depth section and a ramp that has a fixed slope of 1 : 19.85.

For the benchmark simulations we set up a domain ranging from $x_{min} = -10$ m to $x_{max} = 100$ m. The sloping section spans from x_{min} to $x_0 = 19.85$ m. We use a Manning coeffi-

cient $n = 0.01$ to represent the roughness of painted stainless steel wave tank surface. Initial water surface sits at zero elevation, and the initial wave is centered at $x_1 = x_0 + \sqrt{3D/4h} \operatorname{arcosh}(1/0.05)$ so that the wave front just reaches the toe of the beach at the beginning. Initial surface elevation profile $\eta(x, 0)$ and average horizontal velocity $u(x, 0)$ equations are shown in Eq. A.1 and Eq. A.2.

$$\eta(x, 0) = h \operatorname{sech}^2 \left(\sqrt{\frac{3h}{4D}} (x - x_1) \right) \quad (\text{A.1})$$

$$u(x, 0) = -\sqrt{\frac{g}{D}} \eta(x, 0) \quad (\text{A.2})$$

The first case with $h/D = 0.0185$ is presented in Section 4.2.3. Fig. A.1 shows another case of the solitary wave run-up experiment with $h/D = 0.3$. The initial wave height is large enough to result in significant wave breaking, and the wave front becomes nearly vertical as wave breaks and is showing inconsistencies with measured data. This is because the non-dispersive shallow water equations used in the current model could not balance the non-linear effects. Nonetheless, the model does recover the surface profile when wave retreated.

A.2 Analytical Solution of Landslide Generated Tsunami

Liu et al. (2003) obtained analytical solutions of long wave generated by a landslide on a uniform slope with forced linear shallow water equation (Tuck and Hwang, 1972). This

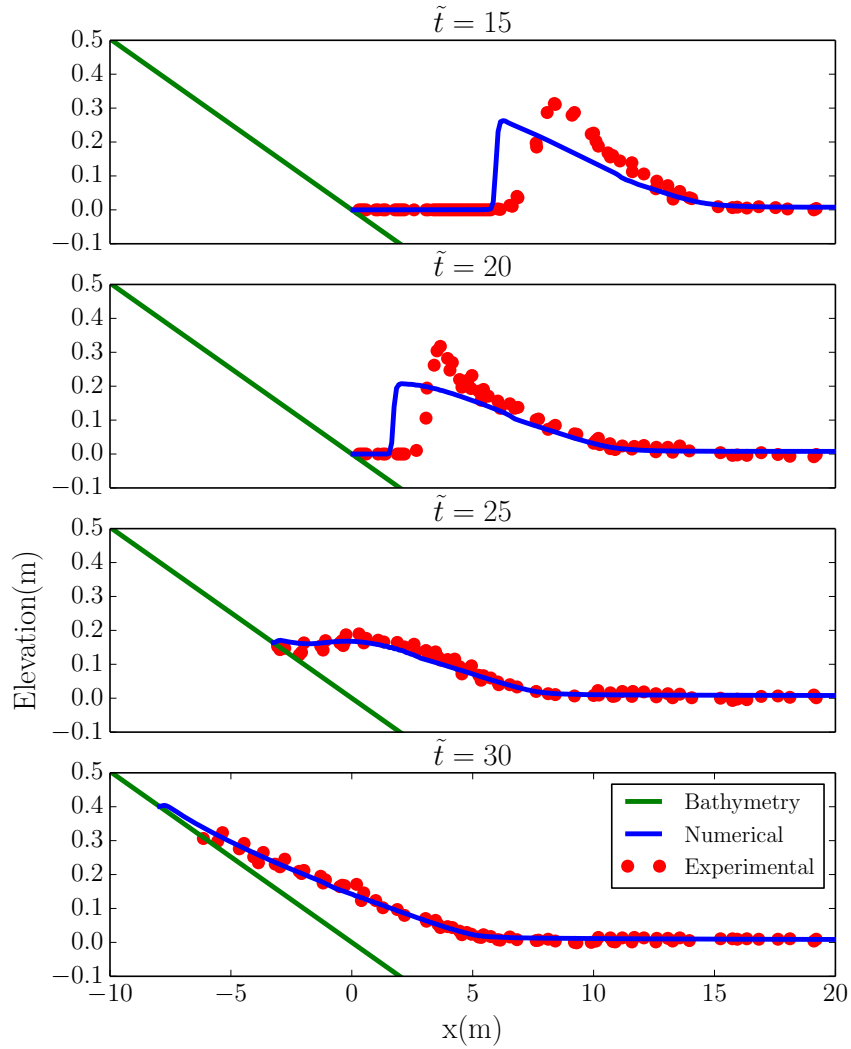


Figure A.1: Comparison between numerical simulation results and experimental data of an $h/D = 0.3$ initial solitary wave. Due to the limitations of the non-dispersive shallow water equations, the model couldn't reproduce the breaking process very well, as is shown in the wave run-up in the top two sub-plots.

problem considers a beach profile $z(x, t)$ with of a fixed bottom $z_0(x)$ and a translating Gaussian landslide body $z_s(x, t)$ (Eq. A.3).

$$\begin{aligned}
 z(x, t) &= z_0(x) + z_s(x, t) \\
 z_0(x) &= -x \tan(\beta) \\
 z_s(x, t) &= \delta \exp \left[- \left(2 * \sqrt{\frac{x\mu^2}{\delta \tan \beta}} - \sqrt{\frac{g}{\delta}} \mu t \right)^2 \right]
 \end{aligned} \tag{A.3}$$

where δ is the vertical maximum slide thickness, β is the constant beach slope, μ is the ratio of thickness and length of the slide (δ/L)

Data is available for two cases:

1. Case A: $\delta = 1$ m, $\beta = 5.7^\circ$, and $\mu = 0.01$
2. Case B: $\delta = 1$ m, $\beta = 5.7^\circ$, and $\mu = 0.1$

We set up a simulation domain of $[0, 5000]$ m with $\Delta x = 2$ m for Case A and $[0, 130]$ m and $\Delta x = 0.1$ m for Case B.

Fig. A.2 and Fig. A.3 present the comparison between the analytical solutions and numerical results at time snapshots of $\tilde{t} = \sqrt{g/\delta}\mu t = 0.5, 1.0, 1.5$ and $0.5, 2.5, 4.5$ for the two cases, respectively. Case A simulation precisely predicts the wave propagation generated by the thin landslide, only except for very small differences close to the shoreline. In contrast, for Case B in Fig. A.3, the numerical surface elevation profile matches the analytical solution relatively well initially, but is showing more and more differences that seem to propagate from

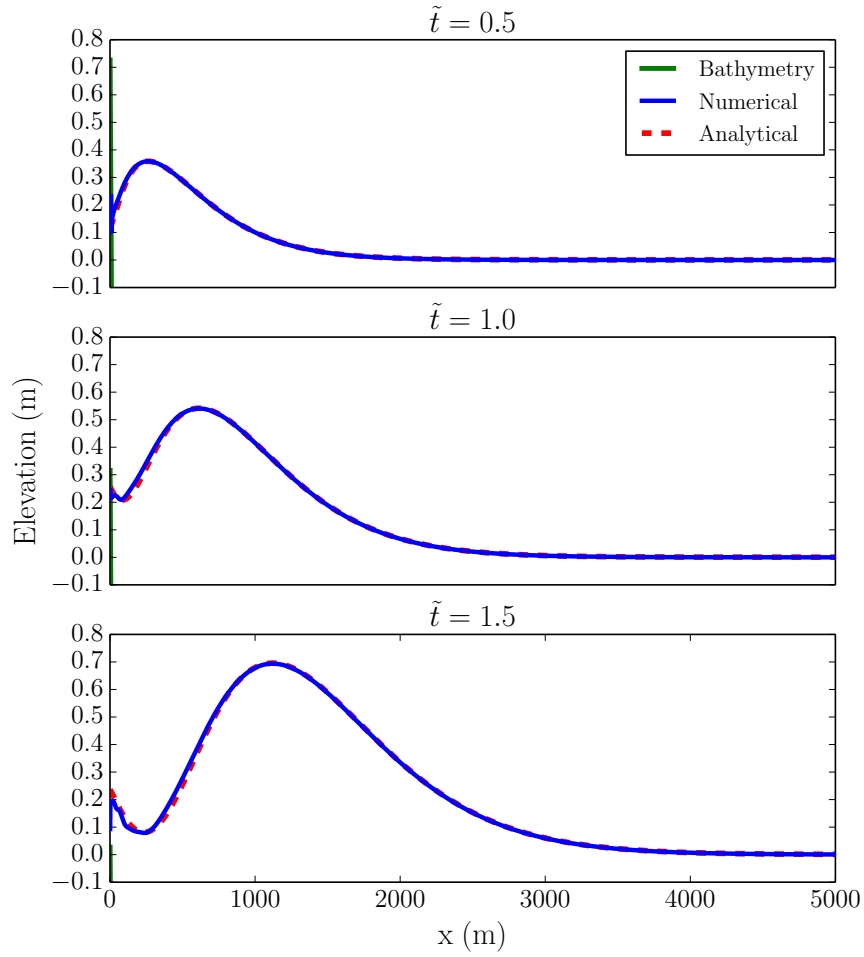


Figure A.2: Comparison between numerical simulation results and analytical solutions of landslide generated tsunami. Case (1).

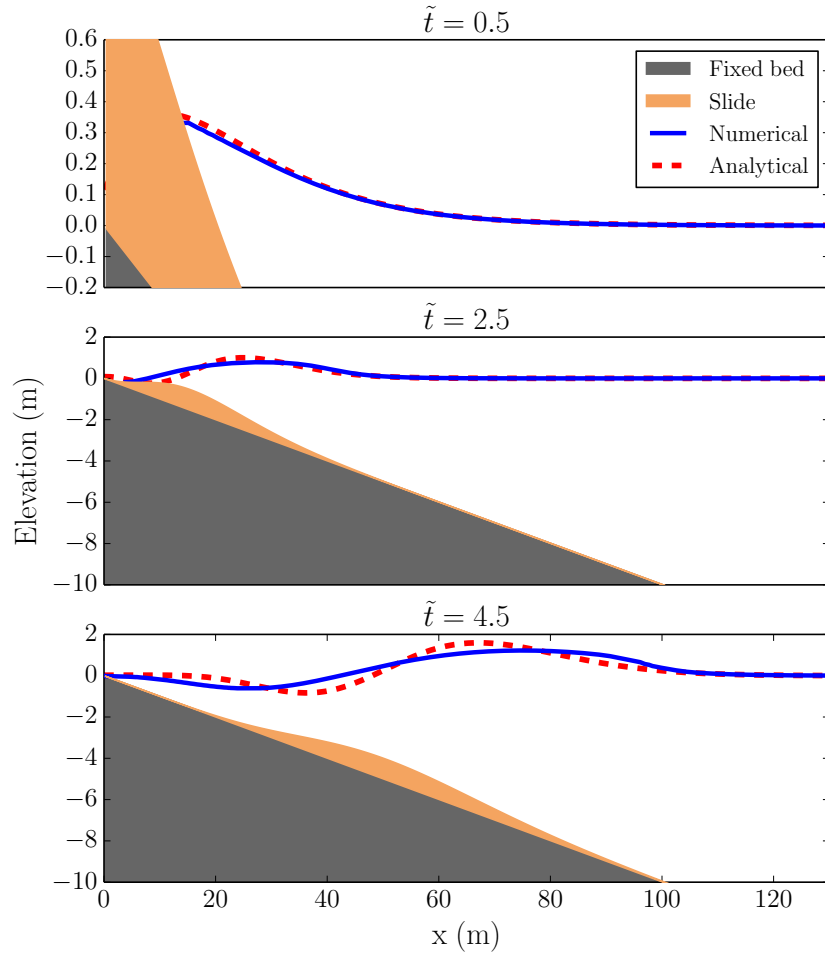


Figure A.3: Comparison between numerical simulation results and analytical solutions of landslide generated tsunami. Case (2).

the shoreline. This is not surprising as we are comparing results from nonlinear numerical model with linear shallow water solutions. The nonlinearity is small at the beginning but becomes dominant later on. The nonlinear effect is hardly noticeable in Case A because the wave height to water depth ratio is very small.